Chapter 3
Calculations of Magnetic Exchange in Multinuclear Compounds

Giang Truong Nguyen and Liviu Ungur

Abstract The magnetic exchange interaction between metal centers in multinuclear compounds plays a defining role in their low-temperature magnetic behavior. Predicting magnetic exchange by computational methods is of high importance for the development of novel magnetic, spintronic materials, and devices that drives further the development of advanced computational methods. In this chapter, we give a brief overview of the origin of magnetic exchange and describe various microscopic theories accounting for it. Several computational approaches which allow the estimation of magnetic exchange in multinuclear compounds are reviewed. Computational challenges of the existing methods for accounting for the magnetic exchange will be discussed in detail in subsequent sections. The combination between accurate on-site eigenstates obtained in ab initio calculations (CASSCF + SOC + ANISO) and theoretical modeling of the magnetic dipole–dipole and exchange interactions within the Lines model, and the recently developed kinetic exchange model is described alongside several recent examples. The last section offers a review of several results obtained recently and gives our perspective on how to achieve an efficient interplay between strong magnetic exchange and a highly axial crystal field on metal sites for designing better exchange-coupled multinuclear single-molecule magnets.

Keywords Magnetic exchange · Broken-symmetry DFT · Ab initio calculations · Magnetic anisotropy · Mechanisms of magnetic interaction · Lines model · Multireference methods

3.1 Origin of Magnetic Exchange

In the language of quantum chemistry, the wave function of a quantum system contains all the required information for the description of its properties. For a many-electron system, the wave function is obtained by solving the electronic Schrodinger equation:

G. T. Nguyen · L. Ungur (✉)
Department of Chemistry, National University of Singapore, Singapore 117543, Singapore
e-mail: chmlu@nus.edu.sg

G. Rajaraman (ed.), *Computational Modelling of Molecular Nanomagnets*, Challenges and Advances in Computational Chemistry and Physics 34,
https://doi.org/10.1007/978-3-031-31038-6_3

$$\mathcal{H}_{\text{elec}}\Phi_{\text{elec}} = E_{\text{elec}}\Phi_{\text{elec}}, \tag{3.1}$$

where

$$\mathcal{H}_{\text{elec}} = \sum_{i=1}^{N} \hat{h}(i) + \sum_{i=1}^{N} \hat{r}_{ij}^{-1}, \tag{3.2}$$

and

$$\begin{aligned} \hat{h}(i) &= \left(-\frac{1}{2}\nabla_i^2 - \sum_A \frac{Z_A}{r_{iA}} \right), \\ \hat{r}_{ij}^{-1} &= \sum_{j>i}^{N} \frac{1}{r_{ij}}. \end{aligned} \tag{3.3}$$

N is the number of electrons in the system, $\hat{h}(i)$ describes the kinetic and nuclear potential energy of the electrons, and r_{12}^{-1} represents the Coulomb repulsion. The antisymmetric principle states that "a many-electron wave function must be antisymmetric with respect to the interchange of the coordinate (both space and spin) of any two electrons", i.e.,

$$\Phi(\mathbf{x_1}, \ldots, \mathbf{x_i}, \ldots, \mathbf{x_j}, \ldots \mathbf{x_N}) = -\Phi(\mathbf{x_1}, \ldots, \mathbf{x_j}, \ldots, \mathbf{x_i}, \ldots \mathbf{x_N}), \tag{3.4}$$

where

$$\Phi(\mathbf{x_1}, \mathbf{x_2}, \ldots, \mathbf{x_N}) = \frac{1}{\sqrt{N!}} \begin{vmatrix} \chi_1(\mathbf{x_1}) & \chi_2(\mathbf{x_1}) & \ldots & \chi_n(\mathbf{x_1}) \\ \chi_1(\mathbf{x_2}) & \chi_2(\mathbf{x_2}) & \ldots & \chi_n(\mathbf{x_2}) \\ \vdots & \vdots & \ddots & \vdots \\ \chi_1(\mathbf{x_n}) & \chi_2(\mathbf{x_n}) & \ldots & \chi_n(\mathbf{x_n}) \end{vmatrix} \tag{3.5}$$

is a Slater determinant. $\chi_i(\mathbf{x_j})$ denotes the molecular orbital i spanned by the electron j. The index $\mathbf{x_j}$ stands for four variables: three spatial $\mathbf{r} = (x, y, z)$ and one spin variable ω of the electron j. Each molecular orbital $\chi(\mathbf{x})$ may be written as a product of a spatial $\psi(r)$ and a spin $\sigma(\omega)$ functions. The spatial (orbital) part describes the position of the electron such that

$$P = \langle \psi_r | \psi_r \rangle = \int |\psi(r)|^2 \mathrm{d}r, \tag{3.6}$$

is the probability of finding the electron in an infinitesimal volume around the position r. The spin of the electron represents an intrinsic angular momentum of the electron and only has two projections along a certain quantization axis (usually z), i.e. [1],

$$\sigma(\omega) = \begin{cases} \alpha(\omega) \\ \beta(\omega), \end{cases} \tag{3.7}$$

and $\alpha(\omega)$ and $\beta(\omega)$ are orthonormal:

$$\begin{aligned} \langle\alpha|\alpha\rangle = \langle\beta|\beta\rangle = \int \alpha^*(\omega)\alpha(\omega) = \int \beta^*(\omega)\beta(\omega) = 1, \\ \langle\alpha|\beta\rangle = \langle\beta|\alpha\rangle = \int \alpha^*(\omega)\beta(\omega) = \int \beta^*(\omega)\alpha(\omega) = 0, \end{aligned} \tag{3.8}$$

where $\alpha(\omega)$ is often used to denote spin *up* ($\uparrow$), while $\beta(\omega)$ denotes spin *down* ($\downarrow$). A molecular orbital is represented as a product between spatial and spin functions:

$$\chi(\mathbf{x}) = \begin{cases} \psi(r)\alpha(\omega) \\ \psi(r)\beta(\omega). \end{cases} \tag{3.9}$$

According to the Pauli exclusion principle, each spatial orbital ψ_r may be populated with a maximum of two electrons with opposite spins. This restriction is nicely embedded into the *Slater Determinant* representation of the multi-electronic wave function (Eq. 3.5) such that the determinant vanishes if two rows/columns are identical. Furthermore, the Slater determinant also ensures the indistinguishability of electrons.

Let us consider a simple system, in which there exist two electrons, whose one-electron wave functions are $\chi_i(\mathbf{r_1}, \omega_1)$ and $\chi_j(\mathbf{r_2}, \omega_2)$. The antisymmetric two-electron wave functions for the whole system are

$$\begin{aligned} \Phi_1(\mathbf{x_1}, \mathbf{x_2}) &= \frac{1}{\sqrt{2}} \left(\psi_i(\mathbf{r}_1)\psi_j(\mathbf{r}_2) - \psi_j(\mathbf{r}_1)\psi_i(\mathbf{r}_2)\right) (\alpha(\omega_1)\alpha(\omega_2)), \\ \Phi_2(\mathbf{x_1}, \mathbf{x_2}) &= \frac{1}{\sqrt{2}} \left(\psi_i(\mathbf{r}_1)\psi_j(\mathbf{r}_2) - \psi_j(\mathbf{r}_1)\psi_i(\mathbf{r}_2)\right) (\beta(\omega_1)\beta(\omega_2)), \\ \Phi_3(\mathbf{x_1}, \mathbf{x_2}) &= \frac{1}{2} \left(\psi_i(\mathbf{r}_1)\psi_j(\mathbf{r}_2) - \psi_j(\mathbf{r}_1)\psi_i(\mathbf{r}_2)\right) (\alpha(\omega_1)\beta(\omega_2) + \alpha(\omega_2)\beta(\omega_1)), \\ \Phi_4(\mathbf{x_1}, \mathbf{x_2}) &= \frac{1}{2} \left(\psi_i(\mathbf{r}_1)\psi_j(\mathbf{r}_2) + \psi_j(\mathbf{r}_1)\psi_i(\mathbf{r}_2)\right) (\alpha(\omega_1)\beta(\omega_2) - \alpha(\omega_2)\beta(\omega_1)). \end{aligned} \tag{3.10}$$

In Φ_1, Φ_2, and Φ_3, the spatial components are antisymmetric with respect to interchange of orbital variables of electrons ($\mathbf{r}_1$ and $\mathbf{r}_2$), while their spin part is symmetric, i.e., the wave functions remain the same, if spins ω_1 and ω_2 are exchanged. In reverse, the spatial component of Φ_4 is symmetric, whereas its spin is antisymmetric. In other words, in the former three wave functions, the spins of the two electrons are parallel to each other ($\uparrow\uparrow$), while in the latter, the electron spins are antiparallel ($\uparrow\downarrow$).

The electronic Hamiltonian for the system is

$$\mathcal{H}_{\text{elec}} = \hat{h}(1) + \hat{h}(2) + \hat{r}_{12}^{-1}. \tag{3.11}$$

The energy of the system, when its wave function is Φ_1, can be calculated as the expectation value of the Hamiltonian:

$$\begin{aligned}
E_1 &= \langle \Phi_1 | \mathcal{H}_{\text{elec}} | \Phi_1 \rangle \\
&= \left\langle \frac{1}{\sqrt{2}}(\psi_i(\mathbf{r}_1)\psi_j(\mathbf{r}_2) - \psi_j(\mathbf{r}_1)\psi_i(\mathbf{r}_2))(\alpha(\omega_1)\alpha(\omega_2)) \right| \hat{h}(1) + \hat{h}(2) + \hat{r}_{12}^{-1} | \\
&\quad \left| \frac{1}{\sqrt{2}}(\psi_i(\mathbf{r}_1)\psi_j(\mathbf{r}_2) - \psi_j(\mathbf{r}_1)\psi_i(\mathbf{r}_2))(\alpha(\omega_1)\alpha(\omega_2)) \right\rangle \\
&= \left\langle \frac{1}{\sqrt{2}}(\psi_i(\mathbf{r}_1)\psi_j(\mathbf{r}_2) - \psi_j(\mathbf{r}_1)\psi_i(\mathbf{r}_2))(\alpha(\omega_1)\alpha(\omega_2)) \right| \hat{h}(1) | \\
&\quad \left| \frac{1}{\sqrt{2}}(\psi_i(\mathbf{r}_1)\psi_j(\mathbf{r}_2) - \psi_j(\mathbf{r}_1)\psi_i(\mathbf{r}_2))(\alpha(\omega_1)\alpha(\omega_2)) \right\rangle \\
&\quad + \left\langle \frac{1}{\sqrt{2}}(\psi_i(\mathbf{r}_1)\psi_j(\mathbf{r}_2) - \psi_j(\mathbf{r}_1)\psi_i(\mathbf{r}_2))(\alpha(\omega_1)\alpha(\omega_2)) \right| \hat{h}(2) | \\
&\quad \left| \frac{1}{\sqrt{2}}(\psi_i(\mathbf{r}_1)\psi_j(\mathbf{r}_2) - \psi_j(\mathbf{r}_1)\psi_i(\mathbf{r}_2))(\alpha(\omega_1)\alpha(\omega_2)) \right\rangle \\
&\quad + \left\langle \frac{1}{\sqrt{2}}(\psi_i(\mathbf{r}_1)\psi_j(\mathbf{r}_2) - \psi_j(\mathbf{r}_1)\psi_i(\mathbf{r}_2))(\alpha(\omega_1)\alpha(\omega_2)) \right| \hat{r}_{12}^{-1} | \\
&\quad \left| \frac{1}{\sqrt{2}}(\psi_i(\mathbf{r}_1)\psi_j(\mathbf{r}_2) - \psi_j(\mathbf{r}_1)\psi_i(\mathbf{r}_2))(\alpha(\omega_1)\alpha(\omega_2)) \right\rangle \\
&= \frac{1}{2}\left\langle \psi_i(\mathbf{r}_1) | \hat{h}(1) | \psi_i(\mathbf{r}_1) \right\rangle + \frac{1}{2}\left\langle \psi_j(\mathbf{r}_1) | \hat{h}(1) | \psi_j(\mathbf{r}_1) \right\rangle \\
&\quad + \frac{1}{2}\left\langle \psi_i(\mathbf{r}_2) | \hat{h}(2) | \psi_i(\mathbf{r}_2) \right\rangle + \frac{1}{2}\left\langle \psi_j(\mathbf{r}_2) | \hat{h}(2) | \psi_j(\mathbf{r}_2) \right\rangle \\
&\quad + \frac{1}{2}\left\langle \psi_i(\mathbf{r}_1)\psi_j(\mathbf{r}_2) | \hat{r}_{12}^{-1} | \psi_i(\mathbf{r}_1) | \psi_j(\mathbf{r}_2) \right\rangle - \left\langle \psi_i(\mathbf{r}_1)\psi_j(r_2) | \hat{r}_{12}^{-1} | \psi_j(\mathbf{r}_1)\psi_i(\mathbf{r}_2) \right\rangle \\
&\quad + \frac{1}{2}\left\langle \psi_j(\mathbf{r}_1)\psi_i(\mathbf{r}_2) | \hat{r}_{12}^{-1} | \psi_j(\mathbf{r}_1) | \psi_i(\mathbf{r}_2) \right\rangle - \left\langle \psi_j(\mathbf{r}_1)\psi_i(\mathbf{r}_2) | \hat{r}_{12}^{-1} | \psi_i(\mathbf{r}_1)\psi_j(\mathbf{r}_2) \right\rangle
\end{aligned} \tag{3.12}$$

It is noteworthy that $\hat{h}(i)$ and $\hat{r}_{12}^{-1}$ are independent of the spin components of electrons and $\hat{r}_{12}^{-1} = \hat{r}_{21}^{-1}$. Therefore, all the spin terms in Eq. 3.12 can be integrated out as

$$\langle \alpha(\omega_1)\alpha(\omega_2) | \alpha(\omega_1)\alpha(\omega_2) \rangle = \langle \alpha(\omega_1) | \alpha(\omega_1) \rangle \langle \alpha(\omega_1) | \alpha(\omega_1) \rangle = 1. \tag{3.13}$$

Using the following notations:

$$\begin{aligned}\left\langle i|\hat{h}|j\right\rangle &= \left\langle \chi_i|\hat{h}|\chi_j\right\rangle = \int d\mathbf{x}_1 \chi_i^*(\mathbf{x}_1) h \chi_j(\mathbf{x}_1),\\ \langle ij|kl\rangle &= \left\langle \chi_i\chi_j|\chi_k\chi_l\right\rangle = \int d\mathbf{x}_1 d\mathbf{x}_2 \chi_i^*(\mathbf{x}_1)\chi_j^*(\mathbf{x}_2) r_{12}^{-1} \chi_k(\mathbf{x}_1)\chi_l(\mathbf{x}_2),\end{aligned} \tag{3.14}$$

one can simplify Eq. 3.12 as

$$E_1 = \left\langle 1|\hat{h}|1\right\rangle + \left\langle 2|\hat{h}|2\right\rangle + \langle 12|12\rangle - \langle 12|21\rangle \tag{3.15}$$

Similarly, the energies corresponding to the other wave functions are

$$\begin{aligned}E_2 &= \langle \Phi_2|\mathcal{H}_{\text{elec}}|\Phi_2\rangle = \left\langle 1|\hat{h}|1\right\rangle + \left\langle 2|\hat{h}|2\right\rangle + \langle 12|12\rangle - \langle 12|21\rangle\,,\\ E_3 &= \langle \Phi_3|\mathcal{H}_{\text{elec}}|\Phi_3\rangle = \left\langle 1|\hat{h}|1\right\rangle + \left\langle 2|\hat{h}|2\right\rangle + \langle 12|12\rangle - \langle 12|21\rangle\,,\\ E_4 &= \langle \Phi_4|\mathcal{H}_{\text{elec}}|\Phi_4\rangle = \left\langle 1|\hat{h}|1\right\rangle + \left\langle 2|\hat{h}|2\right\rangle + \langle 12|12\rangle + \langle 12|21\rangle\,.\end{aligned} \tag{3.16}$$

Based on the calculated results, it is concluded that Φ_1, Φ_2, and Φ_3 are *degenerate*, i.e., $E_1 = E_2 = E_3$ and represent the three components of a spin triplet state ($S = 1$), with projections of the total spin on the z axis as $+1$, -1 and 0, respectively. The state $\Phi_4(\mathbf{x_1}, \mathbf{x_2})$ with energy E_4 corresponds to the total spin singlet ($S = 0$). Because $\langle 12|21\rangle$ is positive, E_4 is larger than $E_{1,2,3}$. Thus, the system's total energy depends on the wave function's total spin. While $\langle 12|12\rangle$ is called Coulomb integral as it corresponds to the Coulomb repulsion between spatial distributions of electrons **1** and **2**, the integral $\langle 12|21\rangle$ does not connect to any classical interpretation and is called *exchange integral*. This exchange integral arises due to a combination of the Coulomb inter-electron repulsion and the antisymmetric nature of the wave functions. Intuitively, one can see the exchange interaction as follows: If two electrons possess different spins, they can share the same spatial component to construct a molecular orbital; on other hand, due to the Pauli exclusion principle, two electrons with the same spin cannot have the same spatial component; thus, there exists a "quantum potential" pushing the same-spin electrons away from each other, which is exchange interaction. By this simple example, one can gain some insights into the origin of exchange interaction. Details about its mechanisms will be discussed in the next section.

In the case of multicenter metal compounds, the frontier (magnetic) electrons residing in 3d or 4f orbitals localized on metal sites weakly interact with each other. The on-site electron repulsion, crystal field, and spin–orbit coupling effects set up the localized wave functions and energy states. The subsequent weak inter-site magnetic exchange establishes the final magnetic configuration of the entire compound. The inter-site exchange integrals $\langle 12|21\rangle$ involving (non-orthogonal) magnetic orbitals (i.e., the orbitals containing paired and unpaired electrons near the HOMO-LUMO

domain) are of major interest since they define the ground state total spin of the investigated system. These integrals are very numerous, even if only ground spin eigenstates of individual sites are used. Non-orthogonality between the local wave functions corresponding to different sites and the spin–orbit effects induce additional exchange mechanisms and, as result, the effective inter-site magnetic exchange interactions may acquire *any* sign: ferro, antiferro, anisotropic character, and even higher-order interaction terms. Thus, the full inter-site magnetic exchange interaction defines the system's ground state. Ferromagnetic interaction leads to the stabilization of the high-spin state, which interacts with the external magnetic field via the Zeeman interaction, whereas antiferromagnetic interaction stabilizes the low-spin ground configuration and thus shows weaker or none Zeeman splitting in an external magnetic field. Given the direct link between exchange interaction and the response to a magnetic field, the name "exchange interaction" is often equivalent to "magnetic interaction".

3.2 Exchange Mechanisms

The theory of exchange interaction was firstly considered by Kramers, developed by Anderson [2–4], and formulated by Goodenough [5–7] and Kanamori [8]. For the last decades, many other authors have elaborated and extended the theory to consider various exchange types in different compounds [9–12]. In this section, we discuss some common exchange mechanisms responsible for promoting magnetic interaction. One of them, which has been observed in many transition-metal compounds, is the direct exchange [13]. It is the direct interaction between magnetic orbitals of interacting magnetic centers that occurs through the space between magnetic sites and becomes important when magnetic centers are relatively close to each other. When open-shell metal sites are relatively distant, the magnetic exchange between them can involve a doubly occupied orbital of a bridging ligand atom. Such mechanism is called *superexchange* and was proposed by Anderson [3, 4, 14–17]. Another mechanism called *double exchange* becomes operative frequently in mixed-valence compounds [18, 19], where the highest occupied molecular orbital (HOMO) is delocalized over several metal sites. Finally, we consider magnetic dipole–dipole interaction [20–23] that is of significance in Ising-like lanthanide-based molecular magnets possessing large uniaxial magnetic moments on individual metal sites.

3.2.1 Direct Exchange

To describe the direct exchange, we examine herein a system containing two magnetic centers, each of them possessing an unpaired electron in a molecular orbital $\psi_{i,j}$. The direct exchange Hamiltonian for the system can be described by the generalized Hubbard model [12, 24, 25]:

$$\mathcal{H}^{\text{direct}}_{\text{Hubbard}} = U_i \hat{n}_{i\alpha}\hat{n}_{i\beta} + U_j \hat{n}_{j\alpha}\hat{n}_{j\beta} + U_{ij} \sum_{\sigma,\sigma'} \hat{n}_{i\sigma}\hat{n}_{j\sigma'} + K_{ij} \sum_{\sigma,\sigma'} \hat{a}^{\dagger}_{i\sigma}\hat{a}^{\dagger}_{j\sigma'}\hat{a}_{i\sigma'}\hat{a}_{j\sigma} + t_{ij} \sum_{\sigma} \left(\hat{a}^{\dagger}_{i\sigma}\hat{a}_{j\sigma} + \hat{a}^{\dagger}_{j\sigma}\hat{a}_{i\sigma}\right), \tag{3.17}$$

where $U_i = \langle ii|ii\rangle, U_j = \langle jj|jj\rangle, U_{ij} = \langle ij|ij\rangle, K_{ij} = \langle ij|ji\rangle$, and $t_{ij} = \left\langle \psi_i|\hat{h}|\psi_j \right\rangle$. $\hat{a}^{\dagger}$ and $\hat{a}$ are creation and annihilation operators, respectively; $\hat{n} = \hat{a}^{\dagger}\hat{a}$ is the occupation number operator; σ and σ' indicate the spin components of the electrons; U_i and U_j are called the on-site Coulomb repulsion when the two electrons occupy the same orbital; U_{ij} is the inter-site Coulomb repulsion when the electrons are in different orbitals; K_{ij} is the exchange integral for the electrons with parallel spins; and t_{ij} is the transfer integral.

The energy difference between the singlet $E(\uparrow\downarrow)$ and triplet $E(\uparrow\uparrow)$ states is as follows:

$$\Delta_{\text{ST}} = E(\uparrow\downarrow) - E(\uparrow\uparrow) = 2K_{ij} - t_{ij}^2 \left(\frac{2}{U_i - U_{ij}} + \frac{2}{U_j - U_{ij}}\right). \tag{3.18}$$

If Δ_{ST} is positive, the energy of the singlet state is higher than that of the triplet, and thus the direct exchange stabilizes the parallel spin alignment. If Δ_{ST} is negative, the direct exchange stabilizes the antiparallel alignment. On the right-hand side of Eq. 3.18, the first term originated from the Coulomb interaction and the Pauli exclusion principle is termed *potential exchange* [4] that favors the ferromagnetic interaction. The second term arising from electron delocalization is *kinetic exchange* [4]. Since the on-site Coulomb interaction (U_i and U_j) is always larger than the inter-site Coulomb interaction (U_{ij}), the second term favors antiferromagnetism. Hence, the competition between these two terms determines whether the direct exchange is ferromagnetic or antiferromagnetic. It is noteworthy that the inter-site transfer integral t_{ij} is strongly dependent on the direct mixing (overlap) between the orbitals, mainly by the kinetic energy operator. The direct exchange has been employed in the theoretical description of transition-metal and radical metal complexes when the magnetic orbitals are relatively diffuse and offer large direct overlap [26–30].

3.2.2 *Superexchange*

To investigate the superexchange mechanism, let us consider a system, where two magnetic centers, each of them containing an electron in a molecular orbital, interact with each other through a doubly occupied (diamagnetic) molecular orbital. This system may be simple, but in fact, the resultant exchange is a combination of multiple exchange mechanisms. Nevertheless, if only superexchange is considered, the Hamiltonian for the system can be represented by the following Hubbard model [31]:

$$\mathcal{H}_{\text{Hubbard}}^{\text{super}} = U_m \left(\hat{n}_{i\alpha}\hat{n}_{i\beta} + \hat{n}_{j\alpha}\hat{n}_{j\beta}\right) + \Delta_{mk}(\hat{n}_{k\alpha} + \hat{n}_{k\beta}) + t_{mk} \sum_{\sigma} \left(\hat{a}_{i\sigma}^{\dagger}\hat{a}_{k\sigma} + \hat{a}_{k\sigma}^{\dagger}\hat{a}_{i\sigma} + \hat{a}_{j\sigma}^{\dagger}\hat{a}_{k\sigma} + \hat{a}_{k\sigma}^{\dagger}\hat{a}_{j\sigma}\right), \tag{3.19}$$

where $m \in \{i, j\}$ denotes the magnetic centers, Δ_{mk} and t_{mk} are the energy gap and the transfer integral between the paramagnetic and diamagnetic orbitals, respectively.

The energy gap between the singlet and triplet states is given as

$$\Delta_{\text{ST}} = -\frac{4t_{mk}^4}{(U_m + \Delta_{mk})^2}\left(\frac{1}{U_m} + \frac{1}{U_m + \Delta_{mk}}\right). \tag{3.20}$$

Since all the terms on the right-hand side of Eq. 3.20 are positive, Δ_{ST} is negative, leading to the antiferromagnetic exchange. If more exchange mechanisms are included in the Hamiltonian (Eq. 3.19), the ferromagnetic contribution can be of significance [5, 6, 32, 33]. Superexchange mechanism has been employed for the description of many lanthanide and transition-metal complexes where the magnetic centers indirectly interact with each other through diamagnetic ligand atoms [34–45].

3.2.3 *Double Exchange*

The double exchange mechanism becomes important in systems where some magnetic electrons can be easily transferred from one metal site to another, a process associated with a change of the metals' oxidation states upon the metal-to-metal charge transfer process. The transferred electron typically does not reside on the bridging ligand atoms [18, 19, 46–49].

Let us consider a two-center system, where each center contains two orbitals. ψ_i and ψ_j are singly occupied while an electron resonates between ψ_i' and ψ_j'. The Hubbard model for this system is [18]:

$$\begin{aligned}\mathcal{H}_{\text{Hubbard}}^{\text{double}} &= (U_i + U_{ij})(\hat{n}_{i'\alpha} + \hat{n}_{i'\beta}) + (U_j + U_{ij})(\hat{n}_{j'\alpha} + \hat{n}_{j'\beta}) \\ &+ K_{ii'} \sum_{\sigma,\sigma'} \hat{a}_{i\sigma}^{\dagger}\hat{a}_{i'\sigma'}^{\dagger}\hat{a}_{i\sigma'}\hat{a}_{i'\sigma} + K_{jj'} \sum_{\sigma,\sigma'} \hat{a}_{j\sigma}^{\dagger}\hat{a}_{j'\sigma'}^{\dagger}\hat{a}_{j\sigma'}\hat{a}_{j'\sigma} \\ &+ t_{i'j'} \sum_{\sigma} (\hat{a}_{i'\sigma}^{\dagger}\hat{a}_{j'\sigma} + \hat{a}_{j'\sigma}^{\dagger}\hat{a}_{i'\sigma}),\end{aligned} \tag{3.21}$$

where the direct exchange between ψ_i and ψ_j is neglected. The pair of electrons in ψ_i and ψ_j are coupled with each other indirectly by the electron resonance between $\psi_{i'}$ and $\psi_{j'}$ (Fig. 3.1). This exchange mechanism is called double exchange and was introduced by Zener [19, 50]. $K_{ii'}$ and $K_{jj'}$ are potential exchange arising from the parallel spins within the same site according to the Hund's rules, and $t_{i'j'}$ is the transfer integral. By assuming the two centers are equivalent, the energy gap between the lowest quartet and doublet states is

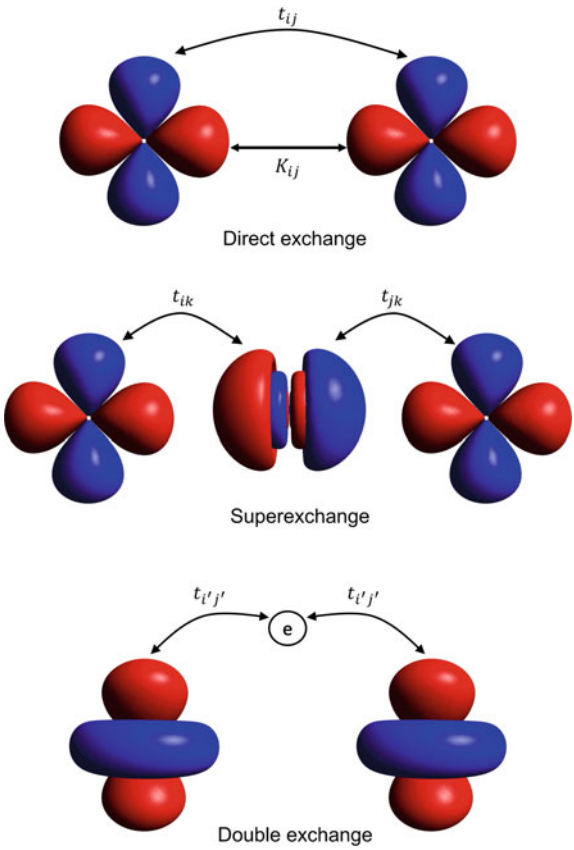

Fig. 3.1 Scheme of various exchange mechanisms in multinuclear compounds

$$\Delta_{\mathrm{QD}} = E(\uparrow\uparrow\uparrow) - E(\uparrow\uparrow\downarrow) = \frac{|t_{i'j'}|}{2}. \tag{3.22}$$

As Δ_{QD} is always positive, the double exchange favors the ferromagnetic coupling between ψ_i and ψ_j.

This result is in contrast to the superexchange mechanism, where ferromagnetic or antiferromagnetic interaction occurs between two atoms with a stable valence (the number of electrons on metal sites does not change).

3.2.4 Magnetic Dipole–Dipole Interaction

Magnetic dipole–dipole interaction refers to the direct interaction between magnetic dipoles localized on different metal sites. Magnetic dipole moment on metal sites is the sum of the spin and orbital momenta as a result of on-site spin–orbit interaction:

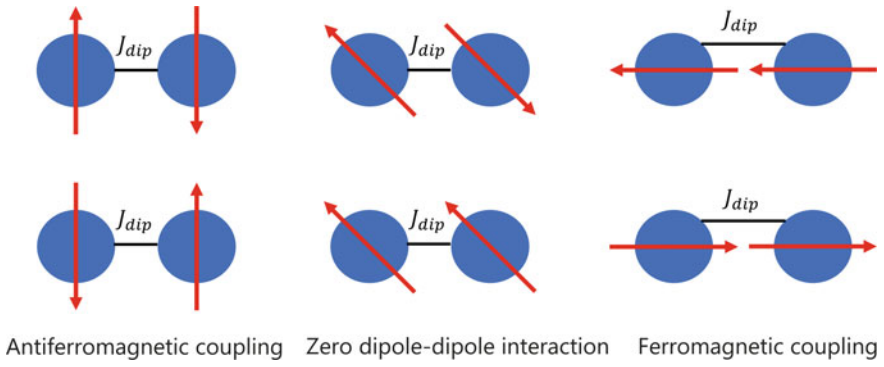

Fig. 3.2 Scheme of various dipole–dipole interactions in multinuclear compounds

$$\vec{\boldsymbol{\mu}} = -\mu_{\mathrm{B}}(\vec{\boldsymbol{L}} + g_{\mathrm{e}}\vec{\boldsymbol{S}}), \tag{3.23}$$

where $\vec{\boldsymbol{L}}$ is the orbital moment admixed via spin–orbit coupling, $g_{\mathrm{e}} \approx 2.0023193$ is the electronic g-factor, $\vec{\boldsymbol{S}}$ is the spin moment, $\mu_{\mathrm{B}} \approx 0.46686448\,[\mathrm{cm}^{-1}/\mathrm{T}]$ is the Bohr magneton.

Suppose $\vec{\boldsymbol{\mu}}_1$ and $\vec{\boldsymbol{\mu}}_2$ are two magnetic dipole moments, localized on two different metal sites. The magnetic dipole–dipole interaction is given by the following Hamiltonian operator:

$$\mathcal{H}_{\mathrm{dip}} = \frac{\mu_{\mathrm{B}}^2[(\vec{\boldsymbol{\mu}}_1\vec{\boldsymbol{\mu}}_2) - 3(\vec{\boldsymbol{\mu}}_1\vec{\boldsymbol{n}}_{12})(\vec{\boldsymbol{\mu}}_2\vec{\boldsymbol{n}}_{12})]}{r_{12}^3}, \tag{3.24}$$

where $\vec{\boldsymbol{n}}_{12}$ is the directional vector connecting the two magnetic dipoles and r_{12} is the distance between them. The dipole–dipole interaction is particularly noticeable in the case when the ground state displays a large orbital contribution to the magnetic moment. As an example, the non-magnetic ground states of Dy_3 triangles and Dy_6 compounds are already set by the dipole–dipole interaction alone [22, 51, 52]. Figure 3.2 shows three cases of the effect of dipole–dipole interaction in uniaxial (Ising) anisotropic metal sites.

Besides, there are other exchange effects arising from spin polarization. These effects correspond to electron excitations within a magnetic center which has been observed occasionally in magnetic resonance experiments [53–57].

3.3 Phenomenological Exchange Hamiltonians

Spin Hamiltonian approach was first introduced by Heisenberg [58] and later discussed by Dirac [59] and Van Vleck [60, 61]. The prerequisite for the derivation and application of this model is that magnetic orbitals are non-degenerate and the spin quantum number S is a good quantum number.

Let us consider a two-center isotropic system in which both of them are characterized by their spins $S_{i,j}$. The Hamiltonian describing the interaction for this system is written as

$$\mathcal{H}_{\text{ex}}^{\text{iso}} = -J_{ij}\hat{S}_i \cdot \hat{S}_j, \tag{3.25}$$

where J_{ij} is an isotropic exchange coupling constant, $\hat{S}_i$ and $\hat{S}_j$ are the spin operators. Since the spin operator for the coupled spin system is $\hat{S} = \hat{S}_i + \hat{S}_j$, the Hamiltonian in Eq. 3.25 can be rewritten as:

$$\mathcal{H}_{\text{ex}}^{\text{iso}} = -\frac{J_{ij}}{2}\left(\hat{S}^2 - \hat{S}_i^2 - \hat{S}_j^2\right), \tag{3.26}$$

where $2\hat{S}_i\hat{S}_j = \hat{S}^2 - \hat{S}_i^2 - \hat{S}_j^2$. When this operator is expanded in the basis of eigenstates of $\hat{S}^2$, $\hat{S}_i^2$, $\hat{S}_j^2$, it is obtained diagonal with the eigenvalues corresponding to the energy levels of the coupled system [62]:

$$E(S) = -\frac{J_{ij}}{2}S(S+1), \tag{3.27}$$

where $S = |S_i - S_j|, |S_i - S_j| + 1, \ldots, S_i + S_j$.

For systems containing more than two magnetic centers, the spin Hamiltonian can be generalized:

$$\mathcal{H}_{\text{ex}}^{\text{iso}} = -\sum_{i<j} J_{ij}\hat{S}_i\hat{S}_j, \tag{3.28}$$

where the sum runs over all the possible pairwise exchange interaction. If J_{ij} is positive, the exchange between S_i and S_j is ferromagnetic. If J_{ij} is negative, the exchange is antiferromagnetic. It is noteworthy that in some contexts, the spin Hamiltonian can be represented in $J\hat{S}_i\hat{S}_j$ or $-2J\hat{S}_i\hat{S}_j$ formalism.

A more general way of expressing magnetic exchange between two interacting spins is given by Eq. 3.29 [54]:

$$\mathcal{H}_{\text{ex}} = \mathbf{S_i} \cdot \mathbf{J} \cdot \mathbf{S_j} = -J_{ij}\hat{S}_i \cdot \hat{S}_j + \hat{S}_i \cdot \mathbf{D}_{ij} \cdot \hat{S}_j + \mathbf{d}_{ij} \cdot \hat{S}_i \times \hat{S}_j, \tag{3.29}$$

where the fully anisotropic interaction matrix $\mathbf{J}$ (3×3 tensor) is decomposed in three terms: First term is the isotropic contribution (J_{ij}, scalar), the second term is the symmetric anisotropic contribution ($\mathbf{D}_{ij}$, 3×3 symmetric matrix), and the last term is the antisymmetric contribution ($\mathbf{d}_{ij}$, 3×3 antisymmetric matrix) [9, 63]. The last two terms represent the anisotropic exchange interaction. In this Hamiltonian, the isotropic term favors either the parallel or antiparallel spin alignment; the symmetric term tends to align the spins along a particular axis; while the antisymmetric term tends to align them perpendicular to each other. For $\hat{S}_{i,j} > 1/2$, higher-order terms such as biquadratic symmetric and antisymmetric terms can be of importance, as well as the zero-field splitting effect on individual metal ions [64].

For strongly anisotropic systems, the spin of the metal sites is not a good quantum number and therefore cannot provide a good description of the ground state. Such situations arise when the spin–orbit coupling on metal sites introduces strong mixing between several low-lying (near-degenerate) spin states. In such cases, the orbital moment is unquenched ($\hat{L} \neq 0$). If this interaction is larger than crystal field, the ground energy multiplet is well characterized by the total angular moment quantum number $\hat{J} = \hat{L} + \hat{S}$. This situation usually occurs in lanthanide and actinide complexes in which the ground multiplet splits into $2J + 1$ energy levels under the influence of ligand field. Owing to the anisotropy within the magnetic ions, the exchange coupling between them is also anisotropic. The anisotropic exchange was first indicated by Stevens [65] and has been developed by Moriya [66] and many others [10, 67–69].

As a result, the spin Hamiltonian is usually incapable to describe the anisotropic exchange interaction. The following approaches are applicable in such circumstances:

- to employ the spin Hamiltonian as in Eq. 3.29 by using the *pseudospins* on metal sites. For example, the pseudospin of Dy^{3+} ion is typically $\tilde{s} = 1/2$ for a Kramers doublet [70], arising from the crystal–field splitting of the ground $J = 15/2$.
- to employ the full total moment J of the ground state of the interacting ions. However, in this case, the number of parameters is very large, and consequently, such J-Hamiltonians are not easily applicable in phenomenological description of experimental data.

The anisotropic exchange between two J-multiplets is far more complex than the isotropic exchange between two S-multiplets. The reason for complexity is the large number of parameters required to describe the on-site crystal field, alongside with a large set of parameters required to describe the full multi-polar exchange interaction. Recently, the J–J exchange was derived analytically by Iwahara [14] which is represented in the following Hamiltonian:

$$\mathcal{H}_{\text{ex}}^{\text{aniso}} = \sum_{kqk'q'} J_{kqk'q'} \frac{O_k^q(\hat{J}_i) O_{k'}^{q'}(\hat{J}_j)}{O_k^0(J_i) O_k^0(J_j)}, \tag{3.30}$$

where $J_{kqk'q'}$ is the exchange coupling constant, $O_k^q(\hat{J}_i)$ and $O_{k'}^{q'}(\hat{J}_j)$ are the extended Stevens operators [71] with rank k and k' and component q and q', respectively. Since $\mathcal{H}_{\text{ex}}^{\text{aniso}}$ is invariant with respect to the time inversion operator, the sum of k and k' is even [72]. As this model corresponds to the direct exchange between the magnetic ions, the exchange constant is the sum of the potential and kinetic contributions:

$$J_{kqk'q'} = J_{kqk'q'}^{\text{PE}} + J_{kqk'q'}^{\text{KE}}. \tag{3.31}$$

The anisotropic exchange between these ions can be reduced to the Ising exchange of two interacting doublets [11, 73]:

$$\mathcal{H}_{\text{ex}}^{\text{Ising}} = -J_{ij}\tilde{s}_{zi} \cdot \tilde{s}_{zj}, \tag{3.32}$$

where $\tilde{s}_{zi}$ and $\tilde{s}_{zj}$ are the projection of the pseudospin operators along the magnetic anisotropic axis. The conditions to obtain the Ising exchange is discussed thoroughly in Ref. [11].

3.4 Computational Approaches for the Estimation of Magnetic Exchange

The computational study of exchange interaction in multinuclear compounds is required to accurately predict low-lying electronic and magnetic properties of the compounds to develop better single-molecule magnets or molecules displaying toroidal magnetization, or estimate structure-property relations, etc. For these purposes, in this section, we will discuss two major classes of computational methods available nowadays for general users: (i) methods based on density functional theory, mainly on the broken-symmetry approach and (ii) methods based on ab initio multiconfigurational wave function theory. In addition, a practical semi-ab initio hybrid approach that is a combination of the ab initio determination of localized wave functions of each metal site and a phenomenological estimation of the magnetic exchange will also be discussed.

3.4.1 Broken-Symmetry Density Functional Theory

Density Functional Theory (DFT) is a very popular computational method [74–78], mostly suitable for cases where the ground state is well characterized by a single Slater determinant, following the fundamental theorems by Hohenberg and Kohn [79]. This method has been adapted for the evaluation of exchange interaction in a broken-symmetry scheme as follows: Consider the case of a weakly exchange-coupled system of two spins $s_{1,2} = 1/2$, the energy of the high-spin configuration $S = 1$ (ferromagnetic coupling) can be directly evaluated since its wave function can be represented by a single determinant ($\Phi(\omega_1, \omega_2) = |\alpha_1\alpha_2\rangle$). On the other hand, the correct wave function of the low-spin state (antiferromagnetic coupling) has a clear multiconfigurational character ($\Phi(\omega_1, \omega_2) = |\alpha_1\beta_2\rangle - |\beta_1\alpha_2\rangle)/\sqrt{2}$) that makes the direct DFT application impractical. In order to overcome this issue, it was proposed to evaluate "a half" of the low-spin wave function, e.g., the energy of the determinant $|\alpha_1\beta_2\rangle$, which is not a true spin eigenstate, and the spin symmetry is no longer retained. To have a practical application, this method makes full use of spin-unrestricted formalism, which means that the spin-up and spin-down molecular orbitals are optimized separately. The exchange parameter for the Heisenberg model $\mathcal{H}_{\text{ex}}^{\text{iso}} = -2\,J\hat{S}_1\hat{S}_2$ is evaluated from the computed results of the two configurations.

For systems containing isotropic magnetic ions, broken-symmetry density functional theory (BS-DFT) has been widely applied for the estimation of exchange interaction [80–84].

There are several formulas allowing to estimate the exchange parameter J from spin-unrestricted BS-DFT calculations [85–89]. Noodleman's equation for J reads [85–87]:

$$J = -\frac{E_{\mathrm{HS}} - E_{\mathrm{BS}}}{S^2_{\mathrm{max}}}, \tag{3.33}$$

where E_{HS} and E_{BS} are the total energies for the fully relaxed high-spin and (broken-symmetry) flipped-spin configurations, while the S^2_{max} is the square of the total spin (maximal value). Yamaguchi proposed the following modified formula [88, 89]:

$$J = -\frac{E_{\mathrm{HS}} - E_{\mathrm{BS}}}{\left\langle \hat{S}^2 \right\rangle_{\mathrm{HS}} - \left\langle \hat{S}^2 \right\rangle_{\mathrm{BS}}}, \tag{3.34}$$

where $\left\langle \hat{S}^2 \right\rangle_{\mathrm{HS}}$ and $\left\langle \hat{S}^2 \right\rangle_{\mathrm{BS}}$ denote the expectation values of the spin-squared operator for the high-spin and flipped-spin wave functions. It is noteworthy that the expectation values might vary significantly from the ones predicted or expected, mainly due to spin contamination problem in spin-unrestricted calculations [90–92].

3.4.1.1 Challenges of BS-DFT Method

The most common issues regarding the application of BS-DFT method are related to the convergence of the self-consistent field optimization for the broken-symmetry configuration [93]. For instance, in dinuclear Co_2^{II} compounds, both Co^{II} ions have a local spin state $S = 3/2$. The spin-flip on one of the Co sites may lead to stabilization of the low-spin ($S = 1/2$) on one, or even on both Co^{II} sites, rather than reversing the full $S = 3/2$ on one of them. The above issue is generally related to the general complexity and multiconfigurational character of the total wave function, mainly when the broken-symmetry configuration is considered. Similar difficulties are met in connection to the evaluation of magnetic exchange in organic bi- and poly-radicals. Another limitation of BS-DFT relates to its inadequacy in describing the intrinsic multiconfigurational nature of the ground states of systems with near-degeneracy and strong spin–orbit coupling effects on individual metal sites. As an example, consider a binuclear Co_2^{II} compound, where both Co^{II} sites are in quasi-O_h symmetry. The ground state of each Co^{II} located in such a ligand environment is a (slightly split) $^4T_2$ state, displaying an effective orbital moment ($\tilde{L} = 1$, i.e., three states with S = 3/2, near-degenerate). A correct wave function for such a ground state requires several Slater determinants, and, therefore, cannot be correctly described by a single-determinant wave function. Consequently, BS-DFT methods may fail in these circumstances [94]. In order to offer a validity test for the BS-DFT wave functions, some software packages (e.g., ORCA [95]) evaluates the overlap

between the orbitals of the high-spin and low-spin configurations [96] following the unique definition of the corresponding orbital transformation [97, 98]. If the BS-DFT calculation is valid, the orbital overlaps are either close to one or zero. In contrast, the calculation cannot be trusted in the case of fractional values of the orbital overlap. It is advised to tighten convergence thresholds for the self-consistent field calculations and carefully inspect the results of BS-DFT calculations, namely the calculated charges and spins on individual atoms. Nevertheless, in spite of all the above challenges, the broken-symmetry approach [85] provides a reasonable approximation for magnetic exchange in compounds containing isotropic magnetic ions [99, 100].

3.4.1.2 A Few Examples of Successful Application of BS-DFT

For systems containing more than two magnetic centers, there are two strategies for BS-DFT: (i) to substitute some of the paramagnetic centers with their diamagnetic analogs in order to simplify the total exchange to a set of pairwise interactions; and (ii) to generalize Yamaguchi's formula by Shoji's approach [101]. As shown in several works, BS-DFT method can accurately determine the sign of the exchange parameter [102]. However, the magnitude of the parameter may be incorrect due to the overestimation of self-interaction error [103, 104].

While the spin quantum number S has been mostly used to quantify the energy states of transition-metal ions, among the paramagnetic trivalent lanthanide ions, only the energy structure of Gd(III) can be represented by its spin. The reason is that the angular momentum of Gd(III) is zero ($L = 0$), resulting in the absence of spin–orbit coupling. A noticeable example is a computational investigation of a dinuclear Gd(III)–Cu(II) complex reported by Rajaraman et al. [105]. The spin Hamiltonian for this two-center system was

$$\mathcal{H}_{\mathrm{ex}}^{\mathrm{iso}} = J\hat{S}_{\mathrm{Gd}}\hat{S}_{\mathrm{Cu}}, \tag{3.35}$$

where $S_{\mathrm{Gd}} = 7/2$ and $S_{\mathrm{Cu}} = 1/2$. The calculated exchange parameter J_{cal} was -5.8 cm^{-1} ($J_{\mathrm{exp}} = -4.42\,\mathrm{cm}^{-1}$). Note that a negative exchange parameter corresponds to ferromagnetic coupling within this Hamiltonian (Eq. 3.35). The report indicated that the account of relativistic effects together with the hybrid B3LYP functional offered an accurate estimation of exchange parameters in this compound [105].

In combination with Molecular Orbital (MO) and Natural Bond Orbital (NBO) analysis, the exchange mechanism in the complex was elucidated in Fig. 3.3. In the Gd(III) center, not only the 4f but also the 5d orbitals play an important role in the magnetic coupling with the Cu(II) ion. The reason for this is that 5d orbitals of the Gd(III) are so diffuse that they gained spin density due to charge transfer from the Cu(II) $3d_{x^2-y^2}$ orbital and spin polarization from the 4f orbitals. This exchange can be considered as a generalization of the Goodenough–Kanamori mechanism [6, 8, 106] giving rise to the ferromagnetic coupling between the magnetic ions. On the other hand, the direct exchange between the 3d and 4f orbitals possessed both ferro- and antiferromagnetic contributions. Due to the symmetry of the complex, two of

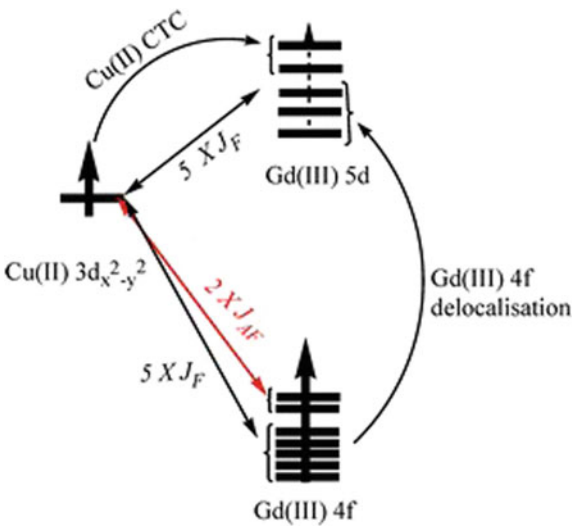

Fig. 3.3 Mechanism for the magnetic coupling in {Gd–Cu} [105]. Printed with permission from Ref. [105]. Copyright 2009, Royal Society of Chemistry

the 4f orbitals overlapping with the $3d_{x^2-y^2}$ gave rise to the kinetic exchange that resulted in the antiferromagnetic coupling. The other five 4f orbitals were orthogonal with the $3d_{x^2-y^2}$ leading to the ferromagnetic coupling via the potential exchange.

Subsequently, the study was extended to a trinuclear Ni(II)–Gd(III)–Ni(II) complex {Ni–Gd–Ni} [107]. The spin Hamiltonian for the system was

$$\mathcal{H}_{\text{ex}}^{\text{iso}} = -J_1 \hat{S}_{\text{Ni}_\text{A}} \hat{S}_{\text{Gd}} - J_2 \hat{S}_{\text{Ni}_\text{B}} \hat{S}_{\text{Gd}} - J_3 \hat{S}_{\text{Ni}_\text{A}} \hat{S}_{\text{Ni}_\text{B}}, \tag{3.36}$$

where $S_{\text{Ni}_\text{A}} = S_{\text{Ni}_\text{B}} = 1$ and $S_{\text{Gd}} = 7/2$. The spin configurations considered in this work are listed in Table 3.1. Despite of the large distance between the two Ni ions, the Ni–Ni exchange could not be neglected because (i) the {Ni–Gd} exchange was weak, and (ii) the {Ni–Ni} exchange could be induced indirectly via the diffuse empty 5d and 6s orbitals of the Gd ion [108, 109]. The computed results showed that the {Ni–Gd} exchange interaction was ferromagnetic with $J_1 \approx J_2$ and the {Ni–Ni} exchange was antiferromagnetic. Both electron delocalization and spin polarization took place in the exchange mechanism (Fig. 3.4). Due to the near orthogonality between the $3d_{x^2-y^2}/3d_{z^2}$ orbitals of the Ni ions and the 4f orbitals of the Gd ion, the antiferromagnetic kinetic exchange in {Ni–Gd} was minor leading to the dominant ferromagnetic interaction. Importantly, the magneto-structural correlation for the {Ni–Gd} exchange was derived that the Ni–O–Gd angles played an important role in the nature of exchange interaction.

Table 3.1 Spin configurations of {Ni–Gd–Ni}

Spin configuration	Ni_A	Gd	Ni_B	Spin number
HS	↑	↑	↑	11/2
BS_1	↓	↑	↑	7/2
BS_2	↑	↑	↓	7/2
BS_3	↓	↑	↓	3/2

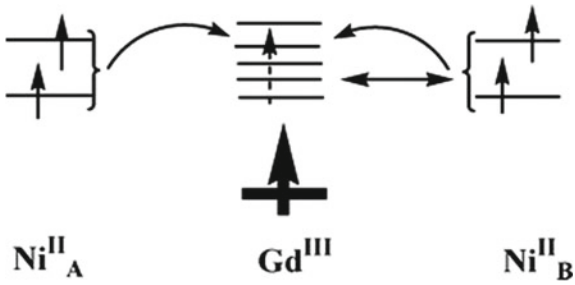

Fig. 3.4 Mechanism for the magnetic coupling in {Ni–Gd–Ni} [107]. Printed with permission from Ref. [107]. Copyright 2009, Royal Society of Chemistry

3.4.1.3 Application of BS-DFT for the Estimation of Magnetic Exchange in Strongly Anisotropic Compounds

As mentioned earlier, the BS-DFT method is applicable for cases when the ground state is well described by a single Slater determinant. This is true for metals ions such as high-spin Fe^{3+}, Gd^{3+}, and Mn^{2+}. However, the method becomes less adequate for metal ions with near-degenerate ground states, e.g., Co^{2+}, Dy^{3+}, Er^{3+}, etc. The low-spin states of compounds containing the latter metal ions have a true multiconfigurational character and orbital near-degeneracy that renders non-negligible spin–orbit coupling to first order of perturbation theory. As a result, their ground states are not characterized by the total spin quantum number, but rather by their *pseudospin* [110]. In order to apply BS-DFT for the estimation of the magnetic exchange in these compounds, the following procedure is proposed:

1. Substitute computationally the strongly anisotropic metal ions by their *spin-isotropic* equivalents, while keeping the ligand frame intact. For instance, Dy^{3+} whose ground state originates from a slight splitting of the free ion ^6H term ($S = 5/2$, $L = 5$) may be computationally replaced by Gd^{3+} which has a clear non-degenerate ground state ^8S term ($S = 7/2$, $L = 0$).
2. Evaluate all magnetic exchange for the metal-substituted compound.
3. Re-scale the exchange parameter for the interacting spins of the original metal ions. For example, the rescaling factor for the magnetic exchange of Dy_2 compound, while evaluated for the substituted compound Gd_2 is

$$J_{\mathrm{Dy-Dy}} = \frac{S_{\mathrm{Gd}}^2}{S_{\mathrm{Dy}}^2} \times J_{\mathrm{Gd-Gd}} = \frac{(7/2)^2}{(5/2)^2} \times J_{\mathrm{Gd-Gd}} = \frac{49}{25} \times J_{\mathrm{Gd-Gd}} \tag{3.37}$$

The above method has been successfully applied in several studies [111–113].

The metal ion substitution can also be a solution for cases where the transition from high-spin configuration to low-spin configuration occurs. There are examples of Mn^{2+} and Fe^{2+} displaying low spin on one metal upon spin-flip in the BS-DFT method. To overcome for this issue, the metal ion may be substituted by, e.g., Cu^{2+}, which has a well-defined $S = 1/2$ in the ground state.

3.4.2 Multiconfigurational Wave Function-Based Methods for Magnetic Exchange

Computational prediction of magnetic exchange by multiconfigurational methods has quite some history. Among first studies refer to the estimation of magnetic exchange in dinuclear Cu_2 complexes through the evaluation of singlet-triplet energy difference [114]. Standard Hartree–Fock calculations gave results that were quite far from the ones extracted from the spin Hamiltonian fitting of the measured magnetism. Configuration interaction and multiconfigurational self-consistent field calculations were applied to further improve the agreement [115–117]. It was reported that the *electron correlation* played a crucial role for the quantitative estimation of spin state energetics of multicenter magnetic compounds and subsequently the magnetic exchange. An accurate account of the electron correlation in exchange-coupled systems is still an open question that further drives the development of novel methods. We may mention here the difference-dedicated configuration interaction (DDCI) method [118] which is a simplified version of the full Configuration Interaction Singles and Doubles (CISD) where excitations that do not contribute directly to the singlet-triplet gaps are eliminated from the CI expansion. In addition, the roles played by various classes of electron excitations were also investigated [115, 116, 119]. While CI methods constitute a systematically improvable approach allowing the calculation of exchange coupling constants through the direct evaluation of spin-state energies [120], their practical application for medium and large molecules is precluded due to the high computational cost required in terms of memory, CPU, and disk space. To some extent, the complications introduced by the (large) basis set expansion of molecular orbitals have been gradually reduced by switching the calculations to either Cholesky representation of bielectronic integrals [121–123] or various methods related to resolution-of-identity (RI) [124] or density fitting (DF) methods alongside with "chains-of-spheres" approaches [125]. More serious difficulties lie in the dimension of the Hilbert space defined by the enlarged active space of the multiconfigurational method. In many cases, the 3d and 4f partly filled orbitals lie at the HOMO-LUMO frontier; therefore, all of them should be included in active space. When following this requirement, the active space grows signifi-

cantly, rendering the number of Slater determinants obtained from the distribution of active electrons among active orbitals too large to handle. Various methodological developments to reduce the number of excitations within a multiconfigurational framework are (i) restricted active space self-consistent field (RASSCF) and (ii) generalized active space self-consistent field (GASSCF) methods [126]. The main idea of these methods is to divide the total active space into several groups of active orbitals while setting the minimum and the maximum number of electrons occupying them. Another alternative to explicitly building a large multiconfigurational wave function is methods based on a different representation of the wave function, for example, density matrix renormalization group or stochastic approaches such as Quantum Monte Carlo. Among the most promising novel correlated methods along this path, we can mention the density matrix renormalization group self-consistent field (DMRG-SCF) [127–131] and its link to multiconfigurational perturbation theory (either NEVPT2 [132] or CASPT2 [133] and their multi-state variants). As an alternative to DMRG-SCF, there are recent reports about spin-adapted Quantum Monte Carlo self-consistent field (FCIQMC-SCF) and promising studies regarding spin state energetics and exchange interactions [134–137]. One of the key advantages offered by these methods is the ability to include a large number of valence orbitals of the metal ions and of the bridging atoms into the variationally optimized active space of the multiconfigurational self-consistent field method. This large active space allows a balanced description of the local crystal field as well as permits a suitable adaptation of the active orbitals as a function of the total spin of the respective states, which are responsible for the inter-center magnetic interaction. The effect of the electron correlation on natural magnetic orbitals [62] is manifold: The magnetic orbitals become slightly larger, offering a slightly larger hybridization with the ligand orbitals, thus improving the accuracy of the local crystal field (and local spin state energies) and indirectly, increasing the role of the superexchange mechanism. Besides, the direct overlap between magnetic orbitals [138] (which are non-orthogonal in the valence bond representation) of neighboring metal sites is also improved by electron correlation, thus increasing the role of the kinetic exchange mechanism. It is expected that electron correlation contributes essentially to the energies of the metal-to-ligand, ligand-to-metal, and metal-to-metal charge transfer configurations, which may contribute to various mechanisms responsible for promoting magnetic exchange [62]. Moreover, electron correlation also contributes to the spin–orbit coupling, as well as the local electric and magnetic dipole moments, which are responsible for the magnetic dipole–dipole interactions (Fig. 3.5).

Herein we briefly review recent work by Bogdanov et al. as an example of the application of modern computational approaches for magnetic exchange in cuprates with corner-sharing CuO_4 plaquettes [137]. The work reported a series of CASSCF/CASPT2 calculations on model cluster fragments [139–141]. The CASSCF was used to account for the static electron correlation, while the CASPT2 was employed to account for the remaining dynamic correlation energy. It is noteworthy that the exchange parameter J_{ex} is strongly dependent on the accuracy of the wave function. The results clearly showed that the obtained wave function could not reproduce the experimental exchange parameters within small active spaces [142–145].

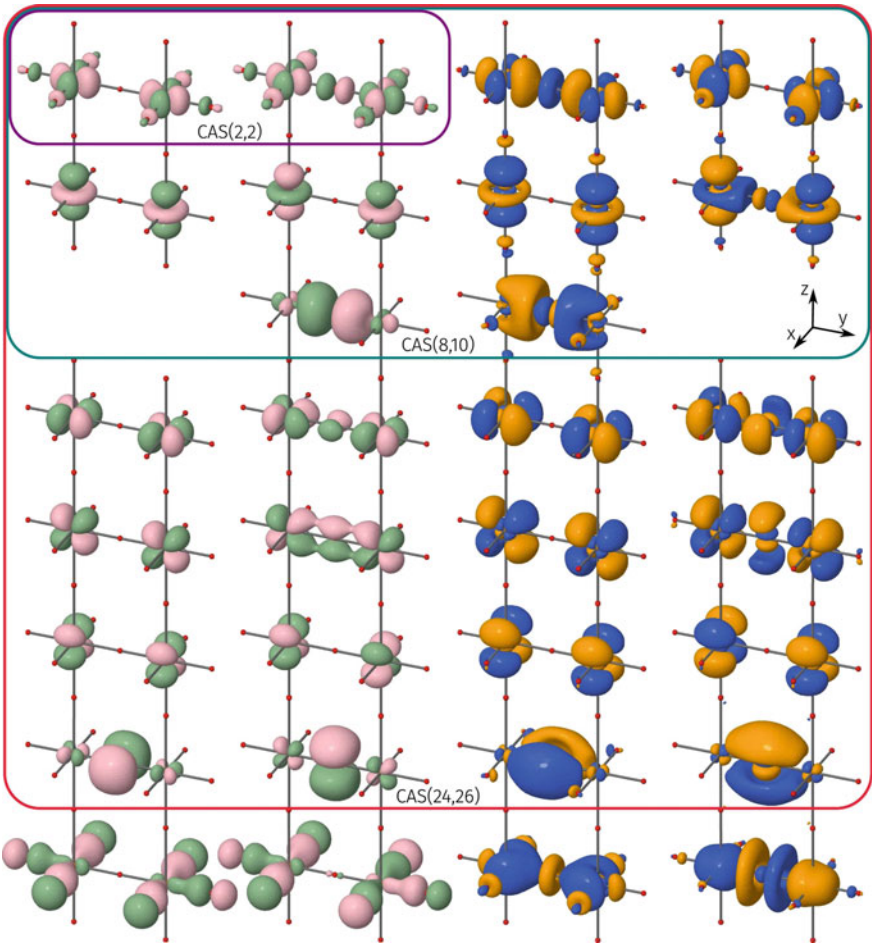

Fig. 3.5 Orbitals in active spaces in CuO_4 [137]

For instance, J_{ex} obtained from CASSCF(2,2) and CASSCF(8,10) was only $\approx 20\%$ and 80% of the experimental data, respectively. To obtain an accurate wave function, the active space was enlarged significantly to consist of all 3d and 4d orbitals of the copper atoms and the 2p and 3p orbitals of the bridging oxygen (CASSCF(24,26)). The wave functions of such a large active space are impossible to optimize (solve) within the CAS framework. Therefore, for this large active space, the authors adapted full configuration interaction quantum Monte Carlo (FCIQMC) [146, 147] and density matrix renormalization group (DMRG) [148, 149] as an approximation. Combined with the multiconfigurational second-order perturbation theory (CASPT2), the obtained exchange parameter J_{ex} was in reasonable good agreement with the corresponding experimental results.

To shed light on the exchange mechanism, the computed results were projected on the following effective Hamiltonian [137]:

$$\begin{aligned} H_{\text{eff}} = & \sum_{\sigma} \left[\sum_{L}^{A,B} \sum_{i=1}^{2} \epsilon_i n_{Li\sigma} + \sum_{i=1}^{2} \sum_{j=1}^{2} t_{ij} \left(c^{\dagger}_{Ai\sigma} c_{Bj\sigma} + c^{\dagger}_{Bi\sigma} c_{Aj\sigma} \right) \right] \\ & + \sum_{L}^{A,B} \left[U_{11} n_{L1\uparrow} n_{L1\downarrow} + U_{22} n_{L2\uparrow} n_{L2\downarrow} + U_{12} \sum_{\sigma\sigma'} n_{L1\sigma} n_{L2\sigma'} \right] \\ & + \sum_{L}^{A,B} \sum_{\sigma} \left(K_1 n_{L1\sigma} + K_2 n_{L2\sigma} \right) \left(c^{\dagger}_{L1\bar{\sigma}} c_{L2\bar{\sigma}} + c^{\dagger}_{L2\uparrow} c_{L1\bar{\sigma}} \right), \end{aligned} \tag{3.38}$$

where only one 3d and one 4d orbital on each copper atom were included. $i = 1, 2$ referred to the 3d and 4d orbital, respectively. Diagonalizing the matrix representation of H_{eff} within a simplified basis set illustrated that the correlated breathing-enhanced hopping mechanism plays an important role in the superexchange in this compound. This breathing mechanism could be essentially thought of as the radial expansion of the 3d orbitals of the copper atoms that was described as a mixing of the 3d and 4d orbitals [150, 151]. The breathing effect reduced the Coulomb energy U but increased the transfer integral t; thus, it strongly influenced the magnitude of the exchange parameter. This was the reason why to accurately describe exchange interaction, the active space was extended to include the 4d orbitals, resulting in CASSCF(24,26) [137]. This ab initio approach was also applied in several other works [25, 152–154].

3.4.2.1 Current Challenges of Correlated Computational Methods for Prediction of Magnetic Exchange

While the new methods are attractive in terms of the number of correlated orbitals, their benchmark for the exchange interaction is yet to be reported. One of the most important challenges of novel computational methods for exchange-coupled systems arises from the fact that the magnetic interaction is quite small in magnitude. As an example, in most lanthanide-based compounds, the magnetic exchange is usually smaller than 1.0 cm^{-1} (1.0 cm^{-1} = 4.55633 $\times$ 10^{-6} Ha = 1.23981 $\times$ 10^{-4} eV = 1.42879 K); while in most transition-metal compounds, magnetic exchange is usually slightly larger, ranging from a few cm^{-1} to about 30 cm^{-1}. Metal-radical compounds usually display larger magnetic exchange interactions. Thus, for any computational method aiming at describing the magnetic exchange correctly, it must be suitable for describing very small energy differences. This requires extremely tight convergence thresholds for optimization of the wave function. For instance, most of the current quantum chemistry programs trigger the convergence of the CI/SCF procedures when the energy difference between two subsequent iterations falls below 10^{-7} Ha (around 0.02 cm^{-1}), which is already on the same energy scale as the

exchange energy states we wish to describe. The situation is even more complicated by various numerical approximations aimed at speeding up the calculations, like Cholesky or RI approaches because all intrinsically possess a certain numerical error.

With respect to electron correlation methods, there is another issue related to *spurious splitting*, which refers to the significant energy splitting between (near-) degenerate orbital states. For high-symmetry compounds, this artificial splitting is usually ignored. However, in the investigation of slight geometrical distortions which break the orbital degeneracy, this spurious splitting becomes problematic, as it is of the same order of magnitude as the true splitting arising from the geometrical distortion. This issue is not only related to the multiconfigurational second-order perturbation theory, but also to cases when the active space of the CASSCF method is increased inconsistently, breaking the balance between ligand and metal orbitals or breaking the symmetry. Another computational issue is related to the large number of spin-coupled states that need to be optimized computationally to offer an accurate account of spin–orbit coupling. This issue is still tractable for transition-metal compounds but falls quickly out of hand in the case of multicenter lanthanide compounds, which are known to require a large number of spin states for spin–orbit interaction already for mononuclear compounds and fragments. Finally, the metal-to-metal, metal-to-ligand, and ligand-to-metal charge transfer states are also required to account for a correct magnetic exchange description. However, computational evaluation of such electronic states is not a trivial task to date.

3.4.3 Semi-ab Initio Approach for the Description of Magnetic Exchange

Given the relatively small magnitude of magnetic exchange in a large class of compounds and the computational difficulties for its accurate evaluation within the multiconfigurational framework, alternative routes were developed. One of the most practical ways to estimate the magnetic exchange of multinuclear strongly anisotropic systems is a hybrid approach that combines multiconfigurational methods with phenomenologic modeling of magnetic exchange. The strategy is as follows:

1. The system is divided into mononuclear fragments. This fragmentation process does not mean removing atoms from the ligand framework, but rather replacing the neighboring metal ions containing open shells by their closest equivalents. It is expected not to alter the low-lying energy structure in each magnetic center significantly.
2. The multiconfigurational ab initio approach (CASSCF/RASSI/CASPT2) is applied to all fragments to obtain an accurate description of their energy structures.
3. The obtained eigenstates of each fragment are then mixed within a suitable exchange model (e.g., the Lines model [155, 156]). In such cases, the parameters of magnetic exchange are obtained empirically by the fitting procedure using the experimental data.

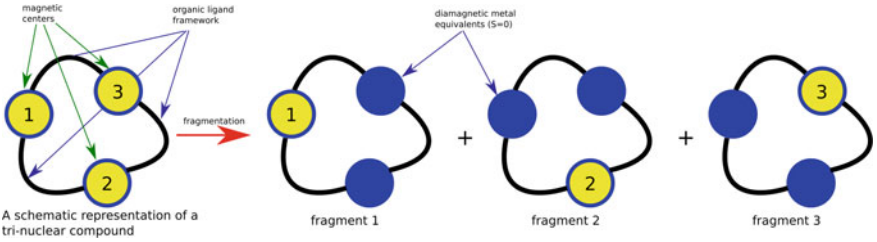

Fig. 3.6 Fragmentation model of a multicenter compound. The scheme shows an overview of a trinuclear compound and the resulting three mononuclear fragments obtained by the *diamagnetic atom substitution* method. By this scheme, the neighboring magnetic centers, containing unpaired electrons are computationally replaced by their diamagnetic equivalents. As an example, divalent transition-metal sites are best replaced by either diamagnetic Zn(II) or Sc(III), in the function that one is the closest by atomic radius and charge. For lanthanides Ln(III), the same principle is applicable, and La(III) or Lu(III) is best suited to replace a given magnetic lanthanide. Individual mononuclear metal fragments are then investigated by common multiconfigurational methods (e.g., CASSCF/CASPT2/RASSI/SINGLE_ANISO). The ab initio results for each fragment are subsequently merged within a suitable model of magnetic exchange, e.g., Lines model [155–157]

4. The energy spectra and magnetic properties of the entire multicenter compound can be computed using the best-fitted parameters of magnetic exchange.
5. As an alternative to the fitting process, the parameters of magnetic exchange may be evaluated using the BS-DFT method, as described above (Fig. 3.6).

3.4.3.1 The Lines Model

The Lines model begins with an effective Heisenberg Hamiltonian when the anisotropic exchange is simplified to isotropic exchange in the absence of spin–orbit coupling [155]:

$$\mathcal{H}_{\text{eff}}^{\text{Lines}} = \sum_{i<j} -J_{ij}\hat{S}_i\hat{S}_j, \tag{3.39}$$

where $\hat{S}_{i,j}$ is the local spin of the ground state on the metal site i, j, respectively. For cases when the local spin–orbit coupling is strong, the effective Hamiltonian is written on the basis of the local *pseudospins*:

$$\mathcal{H}_{\text{eff}}^{\text{Lines}} = -\sum_{i<j} \tilde{J}_{ij}\hat{\tilde{s}}_i\hat{\tilde{s}}_j, \tag{3.40}$$

where $\hat{\tilde{s}}_{i,j}$ is the local pseudospin of the ground state on the metal site i, j, respectively. Given that the local pseudospins are rather anisotropic due to a combined effect of low symmetry and strong spin–orbit coupling effects, the Hamiltonian in

Eq. 3.40 effectively describes the *anisotropic* exchange between the magnetic centers. Its advantage is that only one exchange parameter can represent a single pairwise anisotropic exchange interaction. The Lines model becomes exact in three cases:

- When the two interacting metal sites are isotropic ($g_X = g_Y = g_Z$).
- When the two interacting metal sites are axially anisotropic ($g_X = g_Y = 0$, while $g_Z \neq 0$). In this case, the exchange interaction is of the Ising type.
- When one metal site is isotropic, while the other has an extreme axial anisotropy.

The Lines model is regarded as a suitable approximation for all other cases when the two metal sites have an intermediate anisotropy.

The Lines model has been applied successfully to a variety of compounds [158–160]. The first example is a mixed-valence $Co_3^{II}Co_4^{III}$ heptanuclear wheel [158]. Ab initio fragment calculations revealed that the ground states of all Co^{III} sites has $S = 0$, i.e., are non-magnetic. Similar calculations showed that Co^{II} sites have a ground state characterized by unquenched orbital moment, ${}^4T_2$, split slightly by the low-symmetry components of the crystal field, which deviates from the perfect octahedron. In this case, the spin–orbit interaction is operative in the first order of perturbation theory, leading to a strong mixing of all the three orbital spin $S = 3/2$ states, giving rise to six Kramers doublets. The energy separation between the ground and first-excited Kramers doublet is more than 250 cm^{-1}. The corresponding magnetic exchange Hamiltonian was set as follows:

$$\mathcal{H}_{\text{eff}}^{\text{Lines}} = -J_1\left(\hat{\tilde{s}}_{\text{Co1}}\hat{\tilde{s}}_{\text{Co2}} + \hat{\tilde{s}}_{\text{Co1}}\hat{\tilde{s}}_{\text{Co3}}\right) - J_2\hat{\tilde{s}}_{\text{Co2}}\hat{\tilde{s}}_{\text{Co3}}, \tag{3.41}$$

where $\tilde{s}_{\text{Co1}} = \tilde{s}_{\text{Co2}} = \tilde{s}_{\text{Co3}} = \tilde{s}_{\text{Co(II)}} = 1/2$. The reason for the pseudospin $\tilde{s} = 1/2$ in these Co fragments is the large crystal–field and spin–orbit coupling effects on individual Co sites, leading to a large energy separation between the ground and the first-excited Kramers doublets. This leads to a situation where magnetic exchange interaction couples essentially only the ground Kramers doublets of individual Co sites. In Fig. 3.7, J_1 and J_2 are nearest-neighbor and next-nearest-neighbor exchange parameters, respectively. Intermolecular exchange is considered in the mean-field approximation, simulated by one single parameter zJ', where z represents the number of the surrounding molecules and J' is the average intermolecular exchange parameter [62]. By the simulation of magnetic properties, the computed exchange parameters were found: $J_1 = 1.5$ cm^{-1}, $J_2 = 5.5$ cm^{-1}, and $zJ' = -0.03$ cm^{-1}. Interestingly, the exchange interaction between the distant Co1 and Co3 ions was found much stronger than the interaction between the neighbor Co ions (Co1–Co2 and Co1–Co3). The reason for this surprising effect could originate from the fact that this $Co_3^{II}Co_4^{III}$ complex has two exchange paths with low electron-promotion energy Co(II)–Co(III)–Co(III)–Co(II) that could enhance the exchange between the distant Co(II) centers [161]. Slow magnetization of relaxation was not observed experimentally in this complex even it exhibited strong on-site magnetic anisotropy and inter-site exchange interaction. The lack of single-molecule magnet (SMM) behavior in this compound was explained by the large value of the matrix element of the transverse magnetic moments between the two components of the ground exchange

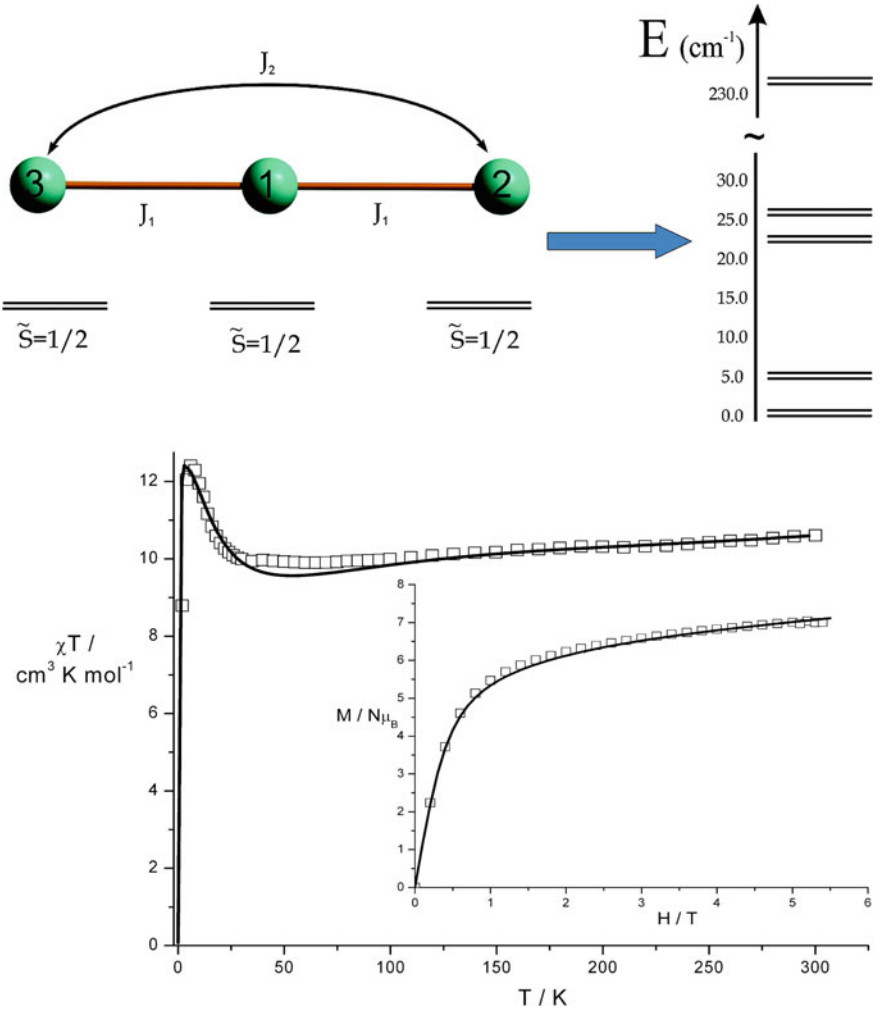

Fig. 3.7 (Top) Exchange scheme in the $Co_3^{II}Co_4^{III}$ complex, (bottom) computed (lines) and experimental (symbols) temperature-dependent magnetic susceptibility, and (inset) molar magnetization of the $Co_3^{II}Co_4^{III}$ complex [158]. Reprinted with permission from Ref. [158]. Copyright 2008, American Chemical Society

states, indicating a pronounced quantum tunneling of magnetization (QTM) [162]. Consequently, it was suggested that for complexes in the weak-exchange limit, i.e., when zero-field splitting is much stronger than exchange interaction, lowering of site symmetry (i.e., enhancing the axiality) might enhance the magnetization blocking behavior.

The Lines model was also applied to multinuclear lanthanide compounds [159, 163–166], for instance, a trinuclear $[Dy_3(Meosalox)_2\ (MeosaloxH)_4\ (X)(Y)]\cdot S$

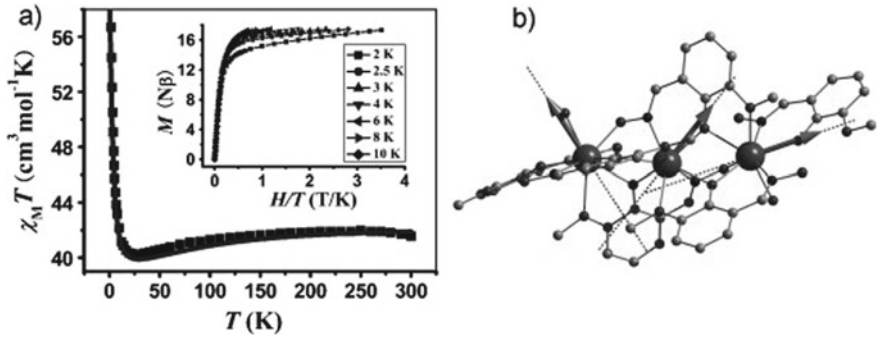

Fig. 3.8 **a** Temperature-dependent magnetic susceptibility, (inset) molar magnetization, and **b** molecular structure of $[Dy_3(Meosalox)_2\ (MeosaloxH)_4\ (X)(Y)]\cdot S$. In **b**, dot lines represent the local anisotropy axes, and arrows illustrate the magnetic moment of each Dy ion [167]. Reprinted with permission from Ref. [167]. Copyright 2011, John Wiley and Sons

(X/Y/S = $OH/H_2O/MeOH\cdot 7H_2O$) complex [167]. Since the energy gap between the ground and first-excited Kramers doublets of the complex was much larger than the exchange splitting, the description of the exchange interaction between the ground J-multiplets was reduced to only the ground doublet on each Dy center. Each of these doublets was represented by the pseudospin $\tilde{s} = 1/2$ [70]. Since the axial component of the ground g-tensor was larger by few orders of magnitude than the transverse components, the magnetic moment of each Dy ion was directed toward its anisotropy axis as shown in Fig. 3.8b. Therefore, the exchange Hamiltonian was close to the Ising model [168, 169]:

$$\mathcal{H}^{\text{Ising}} = -J\left(\tilde{s}_z^{\text{Dy1}}\tilde{s}_z^{\text{Dy2}} + \tilde{s}_z^{\text{Dy1}}\tilde{s}_z^{\text{Dy3}}\right), \tag{3.42}$$

where $\tilde{s}_z^{\text{Dy}i}$ is the projection of the pseudospin along the anisotropy axis of the Dy_i ion. The exchange between the distant Dy ions was neglected. The parameter J was obtained as 7.5 cm^{-1}. By using a single parameter, the computed magnetic susceptibility and molar magnetization in Fig. 3.8a were in reasonable agreement with the experimental data.

Another interesting example is an asymmetric dinuclear $[Dy_2ovph_2Cl_2(MeOH)_3]\cdot$ MeCN complex [20]. Besides exchange coupling, magnetic dipole–dipole interaction also contributes to the magnetic communication between the lanthanide ions. The intramolecular magnetic Hamiltonian becomes

$$\hat{H}_{\text{intra}} = \hat{H}_{\text{exch}} + \hat{H}_{\text{dip}}. \tag{3.43}$$

However, as opposed to magnetic exchange, magnetic dipole–dipole interaction can be computed fully ab initio, using Eq. 3.24 for which all the data are available from fragment calculations. For the case of strong axial anisotropy on metal sites, both exchange and dipolar interactions reduce to Ising magnetic interaction. The

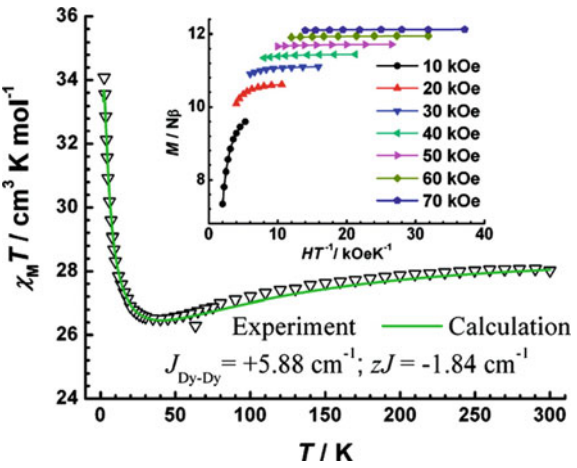

Fig. 3.9 Temperature-dependent magnetic susceptibility and (inset) molar magnetization of $[Dy_2ovph_2Cl_2(MeOH)_3]\cdot MeCN$ [20]. Reprinted with permission from Ref. [20]. Copyright 2011, American Chemical Society

Ising parameters obtained by the fitting procedure in Fig. 3.9 were $J = 5.88$ and $zJ' = -1.84$ cm^{-1}; the Ising dipolar parameter was computed as 5.36 cm^{-1}. In this compound, the intramolecular exchange contributed significantly less ($J_{ex} = 0.52$ cm^{-1}) than the dipole–dipole interaction, such that the ferromagnetic coupling between the Dy ions originated almost entirely from the latter. This phenomenon was attributed to the near parallel alignment of the local magnetic anisotropies [170]. On the other hand, even though the exchange was very weak, it created a bias field efficiently shifting the quantum tunneling steps at zero-field conditions [171, 172].

In $[Cp'_2Dy(\mu\text{-}X)]_2$ (Cp' = cyclopentadienyl-trimethylsilane anion, X = CH_3^-, Cl^-, Br^-, I^-), the exchange interaction was modeled by the following Ising Hamiltonian [173]:

$$\hat{H}_{\text{total}} = -(J_{\text{dip}} + J_{\text{ex}})\hat{s}_{1z}\hat{s}_{2z}, \tag{3.44}$$

where $\hat{s}_z = 1/2$ is the ground pseudospin of the Dy ions. The computed results indicated that both the dipolar and superexchange interactions were significant and antiferromagnetic, which was inversely proportional to the Dy–X bond length. In general, the Lines model has been a great tool in computing the magnetic exchange in Ln complexes as the exchange between them is usually small, and their magnetic anisotropy is very axial [174–176].

The Lines model was also applied for the theoretical study of Dy_3 triangles in Fig. 3.10, which displayed a non-magnetic ground state, quite unexpected for an odd-electron system [177]. Fragment ab initio calculations revealed that (i) the crystal–field splitting of the ground $J = 15/2$ multiplet of each Dy site is quite strong, such that the ground Kramers doublet is well separated from the excited Kramers doublets (about 200 cm^{-1}); (ii) the ground Kramers doublet possesses a very large magnetic anisotropy, $g_X \approx g_Y \approx 0$, while $g_Z \approx 20\mu_B$; (iii) the main magnetic axes of each Dy sites are located almost in the plane of the Dy_3 molecule, making an angle between them $\approx 60°$. The Hamiltonian describing magnetic interaction for the system was

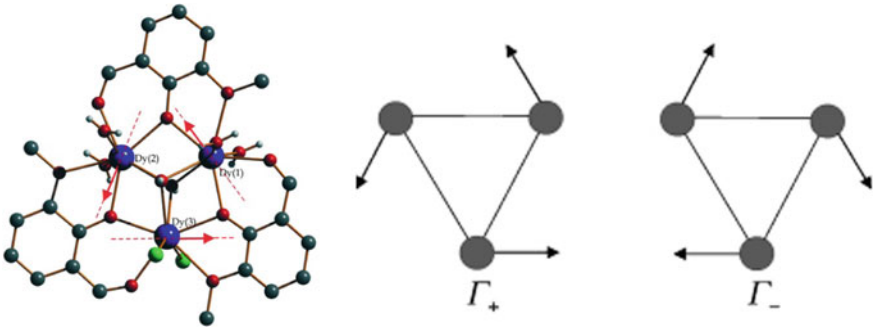

Fig. 3.10 (Left) Molecular structure and (right) the two components of the ground Kramers doublet of the Dy_3 molecule [177]. Reprinted with permission from Ref. [177]. Copyright 2008, John Wiley and Sons

$$\mathcal{H}_{\text{eff}}^{\text{Lines}} = -\sum_{i=1}^{3} J_i \hat{S}_i \hat{S}_{i+1} = -J \sum_{i=1}^{3} \hat{S}_i \hat{S}_{i+1}, \tag{3.45}$$

where $J_i = J$ is an exchange parameter and $S_i = 5/2$ is the spin of the Dy^{III} ions in the absence of the on-site spin–orbit interaction. The addition of the spin–orbit coupling and further diagonalization of the above Hamiltonian gives the exchange spectra and exchange eigenstates for the investigated Dy_3 triangle. Given that the local Kramers doublets were close to $|M_J = \pm 15/2\rangle$ kind and that excited Kramers doublets are much higher in energy with respect to the magnitude of magnetic interaction, the exchange Hamiltonian was expected to be of the Ising type between the local Kramers doublets (non-collinear):

$$\mathcal{H}^{\text{Ising}} = -\tilde{J} \sum_{i=1}^{3} \tilde{s}_{iz} \tilde{s}_{i+1z}, \tag{3.46}$$

where $\tilde{s}_{iz}$ is the z component of the ground state pseudospin. Since $S = 5/2$ and $\tilde{s} = 1/2$,

$$\tilde{J}_i = 25 \cos \phi_{i,i+1} J_i = -12.5 J_i, \tag{3.47}$$

where $\phi_{i,i+1} \approx 2\pi/3$ is the angle between any pair of main axes (Fig. 3.10, $\cos(2\pi/3) = 1/2$). The simulation of magnetic properties in Fig. 3.11 yielded $J = -0.6\,\text{cm}^{-1}$ ($\tilde{J} = +7.5\,\text{cm}^{-1}$). This ferromagnetic exchange stabilizes the local moments in a toroidal fashion, which leads to a cancelation of the total magnetic moment in the ground state. The ground exchange Kramers doublet state consisted of two components, as shown in Fig. 3.10, where all the local magnetic moments were arranged clockwise and anticlockwise, both non-magnetic. These two states Γ_+ and Γ_- in Fig. 3.10 possess a *toroidal* magnetic moment that is oriented *perpendicularly* to the plane of the Dy_3 molecule, τ_+ and τ_-, respectively. As a consequence of the non-magnetic ground state of the molecule, the ground doublet does not inter-

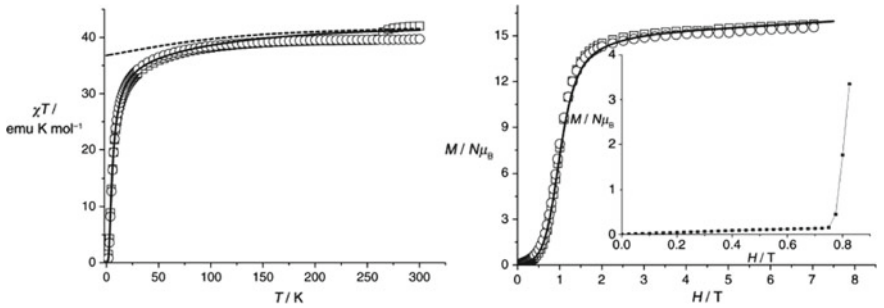

Fig. 3.11 (Left) Magnetic susceptibility and (right) molar magnetization of the Dy_3 molecule [177]. Reprinted with permission from Ref. [177]. Copyright 2008, John Wiley and Sons

act with an external magnetic field applied perpendicularly to the plane of the Dy_3 molecule. However, Zeeman splitting is significant between the excited (magnetic) exchange states for the *in-plane* magnetic fields. Due to the large magnetic moment in the excited exchange states, they quickly become the ground state already for field strengths of about 1.0 T. It is highlighted that molecules displaying stable toroidal moment in the ground states are sought for their potential in quantum computing and information storage since the toroidal state is not perturbed by the neighboring magnetic fields, and as such, may display a long lifetime. Controlling the toroidal states, write-in and read-out, of toroidal information may be undertaken by electric fields [178–180].

Besides this work, the Lines model was also applied to many other complexes to investigate their toroidal magnetic moment. Details about them can be found in Refs. [181–185].

The next class of compounds which has been studied intensively using the model is heterometallic 3d–4f molecules [157, 186–195], for example, a $[Cu_5{}^{II}Dy_4{}^{III}]$ cluster [196]. As the magnetic anisotropy axes of the Dy ions were found to be nearly perpendicular to each other, the magnetic exchange between them was neglected. These results were due to the following reasons: (i) the magnetic anisotropy on the Dy sites offered a nearly Ising exchange and (ii) the parameter of the Ising exchange was $\tilde{J}_{\text{Ising}} = 25 \cos \phi_{1,2} J_{\text{Lines}}$ and $\phi_{1,2} = \pi/2$. Therefore, only three exchange interactions that were supposed to play the dominant role were included in the Lines model:

$$\begin{aligned}\mathcal{H}_{\text{eff}}^{\text{Lines}} = &-J_1(\hat{S}_1^{\text{Dy}}\hat{S}_5^{\text{Cu}} + \hat{S}_1^{\text{Dy}}\hat{S}_8^{\text{Cu}} + \hat{S}_1^{\text{Dy}}\hat{S}_9^{\text{Cu}} + \hat{S}_2^{\text{Dy}}\hat{S}_5^{\text{Cu}} \\ &+ \hat{S}_2^{\text{Dy}}\hat{S}_6^{\text{Cu}} + \hat{S}_2^{\text{Dy}}\hat{S}_7^{\text{Cu}} + \hat{S}_3^{\text{Dy}}\hat{S}_5^{\text{Cu}} + \hat{S}_3^{\text{Dy}}\hat{S}_6^{\text{Cu}} \\ &+ \hat{S}_3^{\text{Dy}}\hat{S}_7^{\text{Cu}} + \hat{S}_4^{\text{Dy}}\hat{S}_5^{\text{Cu}} + \hat{S}_4^{\text{Dy}}\hat{S}_8^{\text{Cu}} + \hat{S}_4^{\text{Dy}}\hat{S}_9^{\text{Cu}}) \\ &- J_2\left(\hat{S}_5^{\text{Cu}}\hat{S}_6^{\text{Cu}} + \hat{S}_5^{\text{Cu}}\hat{S}_7^{\text{Cu}} + \hat{S}_5^{\text{Cu}}\hat{S}_8^{\text{Cu}} + \hat{S}_5^{\text{Cu}}\hat{S}_9^{\text{Cu}}\right) \\ &- J_3\left(\hat{S}_6^{\text{Cu}}\hat{S}_7^{\text{Cu}} + \hat{S}_8^{\text{Cu}}\hat{S}_9^{\text{Cu}}\right),\end{aligned} \tag{3.48}$$

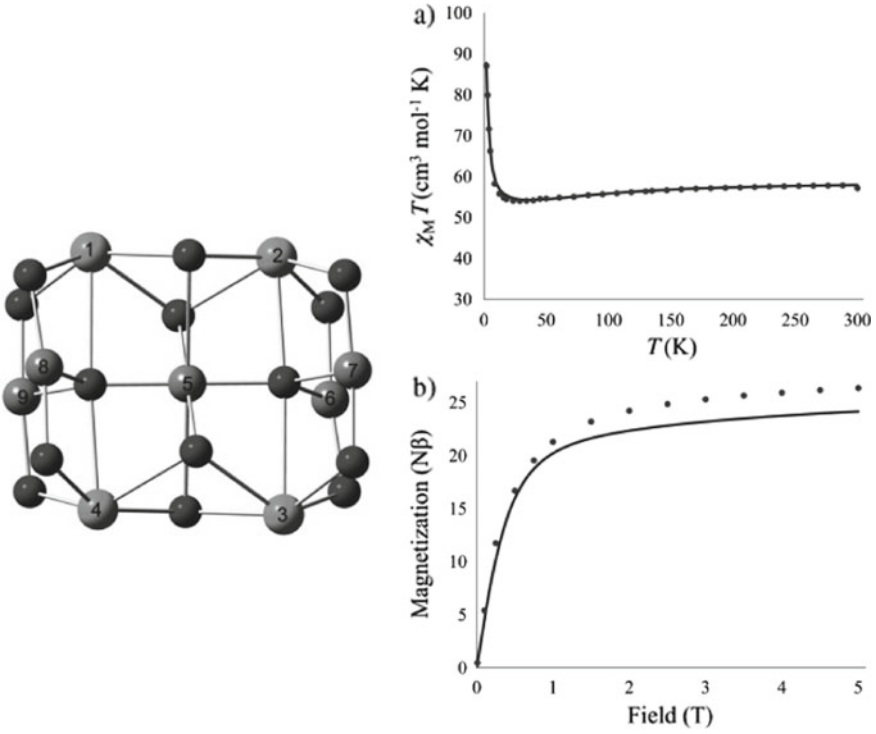

Fig. 3.12 (Left) Computational model and (right) magnetic simulation of $[Cu_5^{II}Ln_4^{III}]$ [196]. Reprinted with permission from Ref. [196]. Copyright 2011, John Wiley and Sons

where the structure of magnetic ions is shown in Fig. 3.12a. Due to the axial nature of the Dy ions, the {Cu–Dy} exchange was approximately Ising type. The obtained exchange parameters were $J_1 = 1.0$ cm^{-1}, $J_2 = 1.3$ cm^{-1} and $J_3 = -4.6$ cm^{-1}. Therefore, the former two interactions were ferromagnetic while the latter was antiferromagnetic. The analysis of the exchange states also indicated that the main magnetic axis of the cluster was almost perpendicular to the Dy_4 plane.

Recently, actinide complexes have attracted some attention in the field of molecular magnetism [197–200]. While their magnetic properties are interesting, the multiconfigurational ab initio studies of them have faced significant challenges due to their intricate electronic structures already for mononuclear actinide compounds [200–206]. The main computational challenges arise due to combined effect of the strong relativistic effects, spin–orbit coupling, and metal-ligand covalency, demanding explicit account of electron correlation. The accuracy of the ab initio calculations refers here not only to the low-lying energy structure but also to the wave functions, electric and magnetic dipole moments, etc., which are challenging for actinide compounds. With respect to the application of the Lines model for the description of magnetism in exchange-coupled actinide compounds, we do not infer any major

problem, except that the strength of the interaction may be stronger compared to exchange-coupled lanthanides. In the case, the local energy structure and magnetic properties of a single actinide ion could be accurately evaluated, then it is possible to apply the Lines model to simulate their exchange interaction.

The Lines model and its applications have been discussed in the above examples. Despite its simplicity, the model has described the exchange coupling quantitatively in a diversity of compounds. Its accuracy strongly depends upon the local energy states calculated by the preceding ab initio methods.

Recently, we have further improved and implemented some *enhanced* versions of the original Lines model in the POLY_ANISO module, which are named LIN3 and LIN9. Their matrix representation is

$$\mathcal{H}_{\text{LIN3}} = (\hat{\tilde{s}}_{X_1}, \hat{\tilde{s}}_{Y_1}, \hat{\tilde{s}}_{Z_1}) \begin{pmatrix} -J_{XX} & 0 & 0 \\ 0 & -J_{YY} & 0 \\ 0 & 0 & -J_{ZZ} \end{pmatrix} \begin{pmatrix} \hat{\tilde{s}}_{X_2} \\ \hat{\tilde{s}}_{Y_2} \\ \hat{\tilde{s}}_{Z_2} \end{pmatrix}, \tag{3.49}$$

$$\mathcal{H}_{\text{LIN9}} = (\hat{\tilde{s}}_{X_1}, \hat{\tilde{s}}_{Y_1}, \hat{\tilde{s}}_{Z_1}) \begin{pmatrix} -J_{XX} & -J_{XY} & -J_{XZ} \\ -J_{YX} & -J_{YY} & -J_{YZ} \\ -J_{ZX} & -J_{ZY} & -J_{ZZ} \end{pmatrix} \begin{pmatrix} \hat{\tilde{s}}_{X_2} \\ \hat{\tilde{s}}_{Y_2} \\ \hat{\tilde{s}}_{Z_2} \end{pmatrix}, \tag{3.50}$$

where the $\hat{\tilde{s}}_{\alpha_i}$ represents the pseudospin on-site i written in its own main axes. The LIN3 and LIN9 models are the extensions of the original Lines model that are more generalized to the full 3×3 exchange matrix in Eq. 3.29. These two models are for cases where the exchange cannot be simplified to the isotropic exchange in the absence of spin–orbit coupling. While these models give more freedom to describe a more complex interaction, these models may face over-parameterization issues, as there are a larger number of parameters involved.

3.4.4 Kinetic Exchange Model

In 2011, a series of N_2^{3-}-radical-bridged dilanthanide complexes [K(18-crown-6]{[$(Me_3Si)_2N]_2$(THF)Ln}$_2(\mu$-$N_2)$] (Ln = Gd (**1-Gd**), Tb (**1-Tb**), Dy (**1-Dy**), Ho (**1-Ho**), Er (**1-Er**)) (Fig. 3.13) was reported [207, 208]. This series has immediately attracted huge attention due to the giant exchange interaction between the Ln^{3+} and N_2^{3-} centers, which is a few orders of magnitude larger than in the conventional complexes. The exchange strength is of the same order as the crystal–field interaction; hence, instead of the ground doublets, the exchange process involves the whole ground J-multiplets [15]. Therefore, the exchange Hamiltonian for the series has to be derived from Eq. 3.30 [14]:

$$\mathcal{H}_{\text{ex}} = \sum_{i=1,2} \sum_{kqq'} J_{kq1q'} \frac{O_k^q(\hat{J}_i)\hat{S}_{q'}}{O_k^0(J_i)S}, \tag{3.51}$$

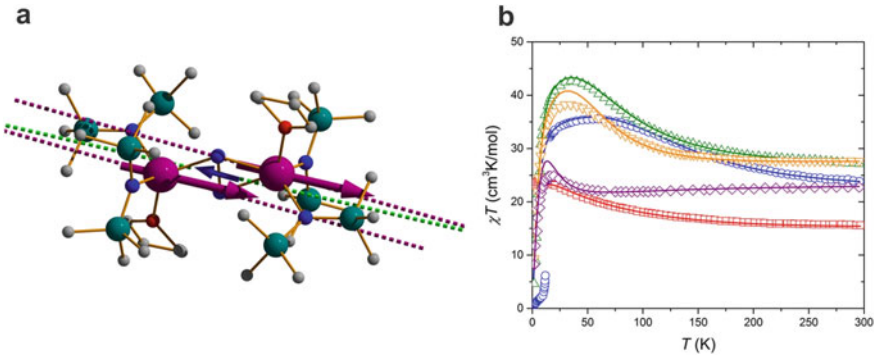

Fig. 3.13 **a** Molecular structure and **b** experimental (symbols) and calculated (lines) magnetic susceptibility of **1-Ln** [15]

which describes the interaction between the total angular momentum J_i of the lanthanide ions ($i = 1, 2$) with the spin $S = 1/2$ of the radical. $J_{kq1q'}$ only accounts for the kinetic exchange as it is usually much stronger than the potential exchange [3, 4]. Due to the D_{2h} symmetry of the magnetic core, the π^* orbital of the radical only overlaps with the $4f_{xyz}$ orbital of the lanthanide ions [15]. Therefore, the maximal rank of k and $|q|$ are 7 and 5, respectively.

The set of $J_{kq1q'}$ was derived by electronic parameters which were obtained from the combination of theoretical models and calculations. The transfer parameter and the energy gap of the 4f and π^* orbitals were extracted from orbital energies in DFT calculations via the tight-binding Hamiltonian:

$$\begin{aligned}\mathcal{H} = \sum_{\sigma}\Bigg[\sum_{i=1,2}\epsilon_{\mathrm{f}}\hat{n}_{i\tilde{\gamma}\sigma} + \epsilon_{\pi^*}\hat{n}_{\pi^*\sigma} \\ + t\left(\hat{a}^{\dagger}_{1\tilde{\gamma}\sigma}\hat{a}_{\pi^*\sigma} + \hat{a}^{\dagger}_{\pi^*\sigma}\hat{a}_{1\tilde{\gamma}\sigma} - \hat{a}^{\dagger}_{2\tilde{\gamma}\sigma}\hat{a}_{\pi^*\sigma} - \hat{a}^{\dagger}_{\pi^*\sigma}\hat{a}_{2\tilde{\gamma}\sigma}\right)\Bigg],\end{aligned} \tag{3.52}$$

where σ, $\hat{n}$, $\hat{a}$, and $\hat{a}^{\dagger}$ are defined in Eq. 3.17; $\tilde{\gamma}$ indicated the Cartesian component of the orbital; ϵ_{f} and ϵ_{π^*} were the energies of the 4f and π^* orbitals, respectively; t and $\Delta = \epsilon_{\pi^*} - \epsilon_{\mathrm{f}}$ were the transfer parameter and $4f - \pi^*$ energy gap, respectively. The diagonalization of the Hamiltonian in Eq. 3.52 resulted in

$$\epsilon_{\mathrm{f,a}} = \epsilon_{\mathrm{f}}, \tag{3.53}$$

$$\epsilon_{\mathrm{f,s}} = \epsilon_{\mathrm{f}} + \frac{1}{2}\left(\Delta - \sqrt{\Delta^2 + 8t^2}\right), \tag{3.54}$$

$$\epsilon_{\pi^*} = \epsilon_{\mathrm{f}} + \frac{1}{2}\left(\Delta + \sqrt{\Delta^2 + 8t^2}\right), \tag{3.55}$$

where a and s denoted the antisymmetric and symmetric orbitals, respectively. Once these orbital energies were obtained from DFT calculations, t and Δ were derived from the above system of equations.

Similarly, the electron-promotion energy from π^* to 4f in **1-Gd** could be derived from the Hubbard Hamiltonian:

$$\begin{aligned}\mathcal{H} = &\sum_{i=1,2}\sum_{\gamma\sigma}\epsilon_{\mathrm{f}}\hat{n}_{i\gamma\sigma} + \sum_{\sigma}\epsilon_{\pi^*}\hat{n}_{\pi^*\sigma} \\ &+ \sum_{\sigma} t\left(\hat{a}^{\dagger}_{1\tilde{\gamma}\sigma}\hat{a}_{\pi^*\sigma} + \hat{a}^{\dagger}_{\pi^*\sigma}\hat{a}_{1\tilde{\gamma}\sigma} - \hat{a}^{\dagger}_{2\tilde{\gamma}\sigma}\hat{a}_{\pi^*\sigma} - \hat{a}^{\dagger}_{\pi^*\sigma}\hat{a}_{2\tilde{\gamma}\sigma}\right) \\ &+ \sum_{i=1,2}\sum_{\langle\gamma\sigma,\gamma'\sigma'\rangle} U_{\mathrm{f}}\hat{n}_{i\gamma\sigma}\hat{n}_{i\gamma'\sigma'} + U_{\pi^*}\hat{n}_{\pi^*\alpha}\hat{n}_{\pi^*\beta} + \sum_{i=1,2}\sum_{\gamma\sigma}\sum_{\sigma'} U_{\mathrm{f},\pi^*}\hat{n}_{\gamma\sigma}\hat{n}_{\pi^*\sigma'},\end{aligned} \tag{3.56}$$

where γ was the component of the 4f orbital; U_{f}, U_{π^*} were on-site, and U_{f,π^*} was inter-site Coulomb repulsion as defined in Eqs. 3.14 and 3.17. The energy gap between the high-spin and low-spin states was

$$\Delta E = E_{\mathrm{LS}} - E_{\mathrm{HS}} = \frac{1}{2}\left(\bar{U} - \sqrt{\bar{U}^2 + 8t^2}\right), \tag{3.57}$$

where

$$\bar{U} = nU_{\mathrm{f}} - \Delta - 2nU_{\mathrm{f},\pi^*}, \tag{3.58}$$

in which, $\bar{U}$ was the averaged promotion energy, and n was the number of 4f electrons in the Ln^{3+} ions. Using the high-spin and low-spin energies obtained from DFT calculations, $\bar{U}$ for **1-Gd** was derived. For the other Ln^{3+} ions, $\bar{U}$ could not be derived in this way owing to their multiconfigurational nature. Nevertheless, $\bar{U}$ was not suitable for the calculation of the exchange parameters since it was just an averaged value and could be inaccurate due to insufficient dynamic correlation in the functional. Therefore, the promotion energy was calculated as follows:

$$U = U_0 + \Delta E_{\alpha}, \tag{3.59}$$

where U_0 was the minimal promotion energy and ΔE_{α} was the excitation energies of the intermediate virtual electron transferred states. The former was obtained from the simulation of experimental magnetic susceptibility, while the latter was approximated as the excitation energies for free Ln^{2+}/Ln^{4+} ions which were computed by the multiconfigurational methods. Substituting t, Δ and U in the formula (Eq. 35 in Ref. [14]) resulted in the set of exchange parameters $J_{kq1q'}$.

The calculated results show that the energy gap between the 4f and π^* orbitals was extremely large ($\Delta \approx 10^4$ cm^{-1}), leading to small promotion energy ($U_0 \approx 10^3$–10^4 cm^{-1}). This was the origin of the giant exchange interaction in this series. Moreover, the $(4f)^n(\pi^*)^1 \Leftrightarrow (4f)^{n-1}(\pi^*)^2$ promotion energy was much larger than that of $(4f)^n(\pi^*)^1 \Leftrightarrow (4f)^{n+1}(\pi^*)^0$; hence, the former process was neglected. The

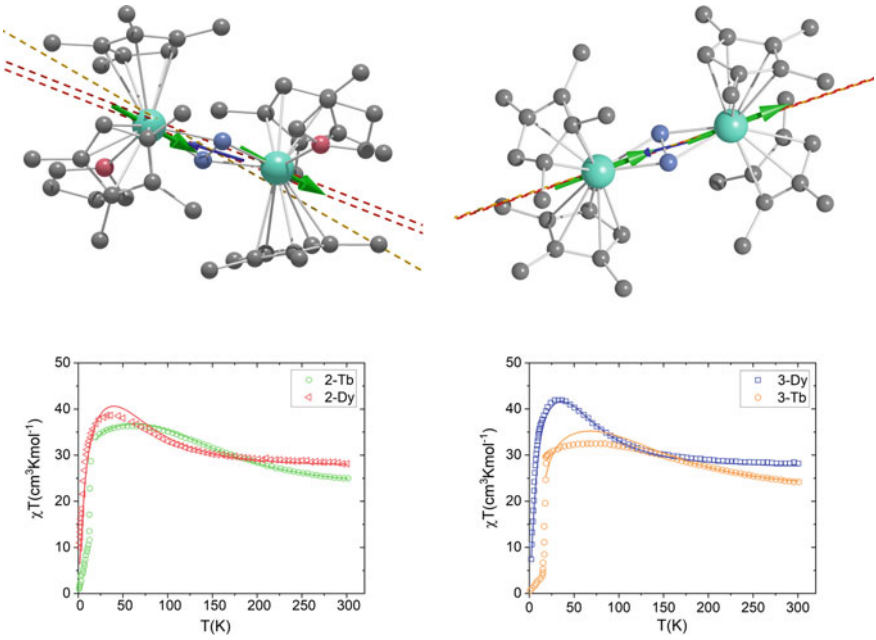

Fig. 3.14 Molecular structure of (top left) **2-Ln** and (top right) **3-Ln**. (Bottom) (lines) calculated and experimental (symbols) temperature-dependent magnetic susceptibility (χT) at $H = 1$ T [16]. Reprinted with permission from Ref. [16]. Copyright 2021, American Chemical Society

trend of the transfer parameter was $t_{Gd} > t_{Tb} > t_{Dy} > t_{Ho} > t_{Er}$ because the higher the atomic number was, the smaller the ionic radius was; thus, the mixing between the orbitals by the kinetic operator decreased. In this exchange model, the only fitting parameter was U_0, whereas the other parameters were derived explicitly.

The analysis of the computed exchange parameters shows that the non-negligible terms were up to rank $k = 7$. The first-rank terms were dominant and isotropic due to the fact that only the $4f_{xyz}$ orbital participated in the exchange process. If the other 4f orbitals are involved, the anisotropy of the first-rank terms will be activated. It is conclusive that the exchange interaction intermixed the ground and excited crystal–field levels on each Ln ion. Therefore, it diminished the magnetic axiality of the low-lying exchange states and restricted the blocking barrier to the first-excited level.

Following by this theoretical study, two other N_2^{3-}-radical-bridged dilanthanide series, which were $[(Cp_2^{Me4H}Ln(THF))_2(\mu\text{-}N_2^{\cdot})]^-$ (THF = tetrahydrofuran, Cp^{Me4H} = tetramethylcyclopentadienyl, Ln = Tb (**2-Tb**), Dy (**2-Dy**)) and $(Cp_2^{Me4H}Ln)_2(\mu\text{-}N_2^{\cdot})]^-$ (Ln = Tb (**3-Tb**), Dy (**3-Dy**)) (Fig. 3.14) [16, 209] were investigated. The kinetic exchange model was applied to these complexes as the magnetic core remained the same. All the electronic parameters were kept fixed except the minimal promotion energy (U_0) which was obtained by the simulation of magnetic properties.

Table 3.2 Experimental (exp) and calculated (cal) blocking energy barriers [16]

	1-Tb	**1-Dy**	**2-Tb**	**2-Dy**	**3-Tb**	**3-Dy**
(exp) U_{eff1}	227	123	242	110	276	108
(cal) U_{eff1}	208	121	240	104	222	113
(exp) U_{eff2}	–	–	–	–	564	–
(cal) U_{eff2}	–	–	–	208	440	210

The computed results indicated that the surrounding ligands did not significantly impact the nature of the exchange interaction provided by the radical. The reason was that the first-rank exchange terms were dominant and isotropic due to the D_{2h} symmetry of the magnetic core. Moreover, in **2-Dy**, **3-Tb**, and **3-Dy**, there existed two blocking energy barriers corresponding to two magnetization relaxation paths. However, the property was only observed experimentally in **3-Tb**. It might be because the measured temperature in the Arrhenius plots for **2-Dy** and **3-Dy** was not high enough to detect the high energy path [16, 209].

As given in Table 3.2, the blocking energy barrier of the Tb congeners is always twice larger than that of the Dy analogs, which appears to be a general property of the N_2^{3-}-radical-bridged complexes. Since the surrounding ligands and the bridging radical are identical, the property must originate from the Ln ions themselves. A thorough examination of the exchange states in **3-Tb** and **3-Dy** showed that the exchange splitting in the Tb complexes is approximately twofold that of the Dy complexes. It is because that (i) the π^* orbital of the radical only overlaps with the $4f_{xyz}$ orbital(s) corresponding to $|L, M_L\rangle = |3, \pm 2\rangle$, and (ii) the kinetic exchange mainly arises from the $(4f)^n(\pi^*)^1 \Leftrightarrow (4f)^{n+1}(\pi^*)^0$ process [14, 15]. As illustrated in Fig. 3.15, for Tb^{3+} ion, there exist two electronic transfer paths; for Dy^{3+}, the orbital $|3, 2\rangle$ is already doubly occupied that the electronic transfer only happens via the other orbital. Thus, the blocking barrier in the Tb complex is around twice larger than in the Dy analog as the magnetization in this family mostly relaxes through the first-excited level [16] (Fig. 3.16).

A subsequent computational investigation of **3-Tb** [17] shows that indeed the Cp ligands lowered the axiality of the complex. The reason was that besides exchange coupling, the N_2^{3-} radical also provided a non-negligible crystal–field effect. As the radical formed the shortest bond with the Tb ions, the magnetic anisotropy axis was oriented by the radical. Thus, the Cp ligands provided the CF effect perpendicular to the anisotropy axis that diminished the axiality of the Tb ions. It is illustrated in Fig. 3.17d that if the crystal field of the surrounding ligands is collinear with the exchange interaction, the axiality will be enhanced significantly. Further analysis highlighted that the ultimate SMM performance of exchange-coupled compounds could be obtained when the crystal field was collinear with the magnetic anisotropy axis while the magnetic exchange was *ferromagnetic* [210, 211]. For this purpose, the energy of the magnetic orbital of the radical needed to be in resonance with the 6s/5d orbitals of the lanthanide to activate the Goodenough mechanism [212]. This

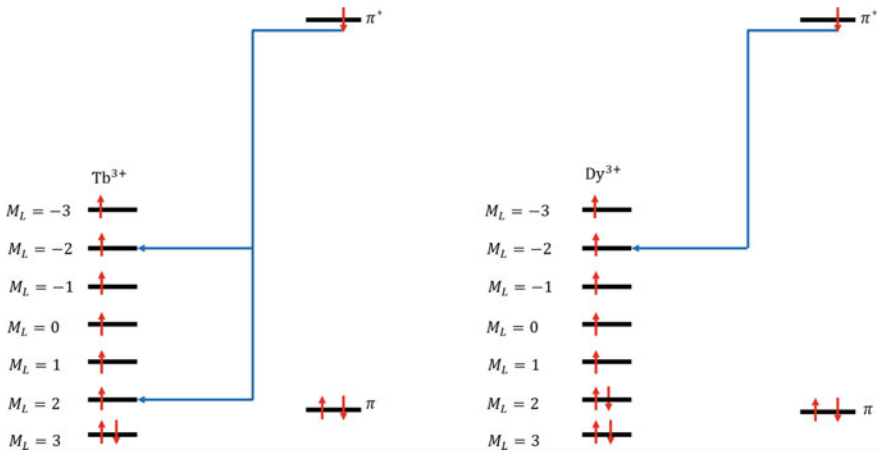

Fig. 3.15 Kinetic exchange path(s) between the π^* orbital and $4f_{xyz}$ orbital(s) in Tb^{3+} and Dy^{3+} ions. For clarity, the splitting between orbitals is not drawn at its true scale [16]. Reprinted with permission from Ref. [16]. Copyright 2021, American Chemical Society

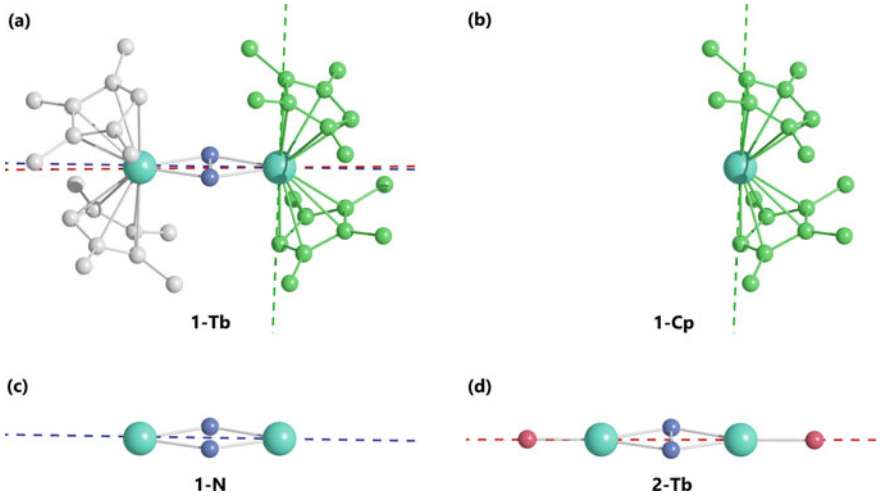

Fig. 3.16 Molecular structures of **a 1-Tb**, **b 1-Cp**, **c 1-N**, and **d 2-Tb** [17]

prediction was recently confirmed by a novel $(Cp^{iPr5})_2Dy_2I_3$ (Cp^{iPr5} = pentaisopropylcyclopentadienyl) complex, which has set the record 100-s blocking temperature of 72 K [213].

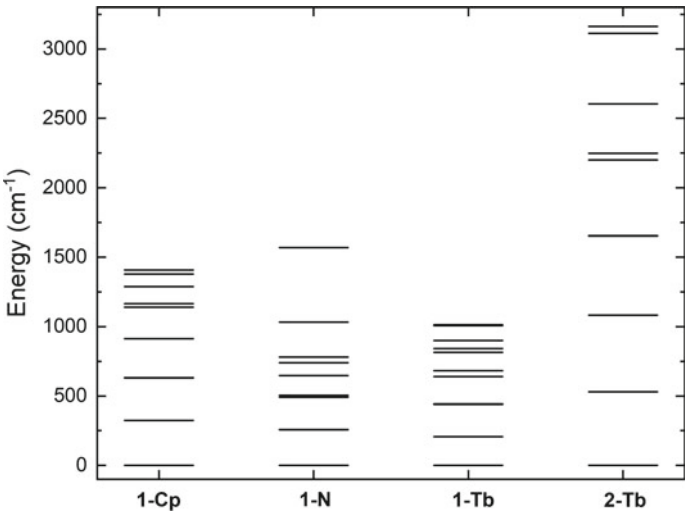

Fig. 3.17 Calculated energies of the ground J-multiplet of the Tb ions (cm^{-1}) [17]. Reprinted with permission from Ref. [17]. Copyright 2022, John Wiley and Sons

3.5 Conclusions

In this chapter, we have introduced the calculation of magnetic exchange in multinuclear compounds from theory to current applications. Several exchange mechanisms have been discussed along with some phenomenological exchange Hamiltonians. Three main approaches for the computational studies of magnetic exchange that have been examined thoroughly are broken-symmetry density functional theory (BS-DFT), multiconfigurational wave function-based methods, and semi-ab initio approach. Each of them has its own advantages and disadvantages that are suitable for different types of complexes. For instance, whereas BS-DFT is very robust, it is not suitable in cases where the ground state is well characterized by a single Slater determinant. Various practical approaches for the application of BS-DFT for deriving magnetic exchange in lanthanide and transition metals are discussed. Several studies where computational magnetic exchange was derived from multiple computational approaches complementing each other are discussed in detail [15, 214]. Besides reviewing various interesting results, we have also pointed out the challenges and limits of current computational methods for predicting magnetic exchange. In conclusion, we hope that this chapter will stand as a motivation for the development of novel computational methods, aiming at accurate description of electronic structure and properties of exchange-coupled systems, for the ultimate dream of computational prediction of electronic structure and properties of multicenter multifunctional materials.

References

1. Szabo A, Szabo A, Ostlund N (1982) Modern quantum chemistry: introduction to advanced electronic structure theory. Macmillan
2. Anderson P (1950) Phys Rev 79:350
3. Anderson PW (1959) Phys Rev 115:2–13
4. Anderson PW (1963) Solid State Phys 14:99–214
5. Goodenough JB (1955) Phys Rev 100:564
6. Goodenough JB (1958) J Phys Chem Solids 6:287–297
7. Goodenough JB (1963) Magnetism and the chemical bond, vol 1. Interscience Publishers
8. Kanamori J (1959) J Phys Chem Solids 10:87–98
9. Moriya T (1960) Phys Rev 120:91
10. Levy PM (1964) Phys Rev 135:A155
11. Chibotaru LF, Iwahara N (2015) New J Phys 17:103028
12. Ceulemans A, Chibotaru L, Heylen G, Pierloot K, Vanquickenborne L (2000) Chem Rev 100:787–806
13. Freeman A, Watson R (1961) Phys Rev 124:1439
14. Iwahara N, Chibotaru LF (2015) Phys Rev B 91:174438
15. Vieru V, Iwahara N, Ungur L, Chibotaru LF (2016) Sci Rep 6:24046
16. Nguyen GT, Ungur L (2021) Phys Chem Chem Phys 23:10303–10310
17. Nguyen GT, Ungur L (2022) Chem Eur J e202200227
18. Anderson PW, Hasegawa H (1955) Phys Rev 100:675
19. De Gennes P-G (1960) Phys Rev 118:141
20. Guo Y-N, Xu G-F, Wernsdorfer W, Ungur L, Guo Y, Tang J, Zhang H-J, Chibotaru LF, Powell AK (2011) J Am Chem Soc 133:11948–11951
21. Landi GT (2014) Phys Rev B 89:014403
22. Ungur L, Lin S-Y, Tang J, Chibotaru LF (2014) Chem Soc Rev 43:6894–6905
23. Das C, Upadhyay A, Vaidya S, Singh SK, Rajaraman G, Shanmugam M (2015) Chem Commun 51:6137–6140
24. Hubbard J (1963) Proc R Soc Lond Ser A Math Phys Sci 276:238–257
25. Malrieu JP, Caballol R, Calzado CJ, de Graaf C, Guihery N (2014) Chem Rev 114:429–492
26. Coronado E, Galán-Mascarós JR, Giménez-Saiz C, Gómez-García CJ, Triki S (1998) J Am Chem Soc 120:4671–4681
27. Desplanches C, Ruiz E, Rodríguez-Fortea A, Alvarez S (2002) J Am Chem Soc 124:5197–5205
28. Blanchet-Boiteux C, Mouesca J-M (2000) J Phys Chem A 104:2091–2097
29. Calzado CJ, Cabrero J, Malrieu JP, Caballol R (2002) J Chem Phys 116:3985–4000
30. Calzado CJ, Malrieu J-P (2001) Phys Rev B 63:214520
31. Van den Heuvel W, Chibotaru L (2007) Phys Rev B 76:104424
32. Kugel K, Khomskij D (1972) Zh Ehksp Teor Fiz Pis'ma Red 15:629–632
33. Tokura Y, Nagaosa N (2000) Science 288:462–468
34. Lin P-H, Burchell TJ, Ungur L, Chibotaru LF, Wernsdorfer W, Murugesu M (2009) Angew Chem Int Ed 48:9489–9492
35. Vieru V, Pasatoiu TD, Ungur L, Suturina E, Madalan AM, Duhayon C, Sutter J-P, Andruh M, Chibotaru LF (2016) Inorg Chem 55:12158–12171
36. Roubeau O, Clérac R (2008) Eur J Inorg Chem 2008:4325–4342
37. Osa S, Kido T, Matsumoto N, Re N, Pochaba A, Mrozinski J (2004) J Am Chem Soc 126:420–421
38. Alexandru M-G, Visinescu D, Shova S, Lloret F, Julve M (2017) Inorg Chem 56:12594–12605
39. Onofrio N, Mouesca J-M (2010) J Phys Chem A 114:6149–6156
40. Van den Heuvel W, Chibotaru LF (2007) Phys Rev B 76:104424
41. Hou X, Nguyen GT, Xu T, Wei H, Herng TS, Huo G, Wang D, Ding J, Wu S, Ungur L et al (2022) Chem Eur J e202200687

42. You M, Nguyen GT, Shao D, Wang T, Chang X-Y, Ungur L, Zhang Y-Z (2022) Dalton Trans 51:5596–5602
43. Zhou J-S, Alonso JA, Pomjakushin V, Goodenough JB, Ren Y, Yan J-Q, Cheng J-G (2010) Phys Rev B 81:214115
44. Zhang J, Cai X, Xia W, Liang A, Huang J, Wang C, Yang L, Yuan H, Chen Y, Zhang S, Guo Y, Liu Z, Li G (2019) Phys Rev Lett 123:047203
45. Magnani N, Colineau E, Eloirdi R, Griveau J-C, Caciuffo R, Cornet S, May I, Sharrad C, Collison D, Winpenny R (2010) Phys Rev Lett 104:197202
46. Motome Y, Furukawa N (2001) J Phys Soc Jpn 70:1487–1490
47. Azhar M, Mostovoy M (2017) Phys Rev Lett 118:027203
48. Veiga L, Fabbris G, Van Veenendaal M, Souza-Neto N, Feng H, Yamaura K, Haskel D (2015) Phys Rev B 91:235135
49. Ono A, Ishihara S (2017) Phys Rev Lett 119:207202
50. Zener C (1951) Phys Rev 82:403
51. Ungur L, Langley SK, Hooper TN, Moubaraki B, Brechin EK, Murray KS, Chibotaru LF (2012) J Am Chem Soc 134:18554–18557
52. Ungur L, Chibotaru LF (2011) Phys Chem Chem Phys 13:20086–20090
53. Coronado E, Delhaès P, Gatteschi D, Miller JS (2013) Molecular magnetism: from molecular assemblies to the devices, vol 321. Springer Science & Business Media
54. Gatteschi D, Sessoli R, Villain J (2006) Molecular nanomagnets. Oxford University Press, Oxford
55. Zhang S, Levy P, Fert A (2002) Phys Rev Lett 88:236601
56. Logemann R, Rudenko AN, Katsnelson MI, Kirilyuk A (2017) J Phys Condensed Matter 29:335801
57. Jia C, Onoda S, Nagaosa N, Han JH (2007) Phys Rev B 76:144424
58. Heisenberg W (1926) Z Phys 38:411–426
59. Dirac PAM (1929) Proc R Soc Lond Ser A 123:714–733
60. Van Vleck JH (1932) Electric and magnetic susceptibilities. Clarendon Press
61. Van Vleck JH (1945) Rev Mod Phys 17:27
62. Kahn O (1993) Molecular magnetism. VCH Publishers, New York
63. Dzyaloshinsky I (1958) J Phys Chem Solids 4:241–255
64. Plumer M (2007) Phys Rev B 76:144411
65. Stevens K (1953) Rev Mod Phys 25:166
66. Moriya T (1960) Phys Rev 120:91
67. Birgeneau R, Hutchings M, Baker J, Riley J (1969) J Appl Phys 40:1070–1079
68. Elliott R, Thorpe M (1968) J Appl Phys 39:802–807
69. Santini P, Carretta S, Amoretti G, Caciuffo R, Magnani N, Lander GH (2009) Rev Mod Phys 81:807
70. Chibotaru LF, Ungur L (2012) J Chem Phys 137:064112
71. Stevens K (1952) Proc Phys Soc Sect A 65:209
72. Abragam A, Bleaney B (2012) Electron paramagnetic resonance of transition ions. Oxford University Press, Oxford
73. Abragam A, Bleaney B (1970) Electron paramagnetic resonance of transition ions. Claredon Press, Oxford
74. Neese F (2009) Coord Chem Rev 253:526–563
75. Bencini A, Totti F, Daul CA, Doclo K, Fantucci P, Barone V (1997) Inorg Chem 36:5022–5030
76. Comba P, Hausberg S, Martin B (2009) J Phys Chem A 113:6751–6755
77. Ruiz E (2011) J Comput Chem 32:1998–2004
78. Peralta JE, Melo JI (2010) J Chem Theory Comput 6:1894–1899
79. Hohenberg P, Kohn W (1964) Phys Rev 136:B864–B871
80. Miller JS, Drillon M (2001) Magnetism: molecules to materials IV, vol 4. Wiley
81. Piligkos S, Rajaraman G, Soler M, Kirchner N, van Slageren J, Bircher R, Parsons S, Güdel H-U, Kortus J, Wernsdorfer W et al (2005) J Am Chem Soc 127:5572–5580
82. Ruiz E, Cano J, Alvarez S, Alemany P (1999) J Comput Chem 20:1391–1400

83. Ruiz E, Rodríguez-Fortea A, Cano J, Alvarez S, Alemany P (2003) J Comput Chem 24:982–989
84. Caballol R, Castell O, Illas F, Moreira IDPR, Malrieu JP (1997) J Phys Chem A 101:7860–7866
85. Noodleman L (1981) J Chem Phys 74:5737–5743
86. Ginsberg A (1980) J Am Chem Soc 102:111–117
87. Noodleman L, Davidson ER (1986) Chem Phys 109:131–143
88. Yamaguchi K, Fukui H, Fueno T (1986) Chem Lett 15:625–628
89. Soda T, Kitagawa Y, Onishi T, Takano Y, Shigeta Y, Nagao H, Yoshioka Y, Yamaguchi K (2000) Chem Phys Lett 319:223–230
90. Baker J, Scheiner A, Andzelm J (1993) Chem Phys Lett 216:380–388
91. Menon AS, Radom L (2008) J Phys Chem A 112:13225–13230
92. Montoya A, Truong TN, Sarofim AF (2000) J Phys Chem A 104:6108–6110
93. Orio M, Pantazis DA, Neese F (2009) Photosynth Res 102:443–453
94. Ghosh A (2006) JBIC J Biol Inorg Chem 11:712–724
95. Neese F (2018) WIREs Comput Mol Sci 8:e1327
96. Neese F (2004) J Phys Chem Solids 65:781–785
97. Amos AT, Hall GG, Jones H (1961) Proc R Soc Lond Ser A Math Phys Sci 263:483–493
98. King HF, Stanton RE, Kim H, Wyatt RE, Parr RG (1967) J Chem Phys 47:1936–1941
99. Hegetschweiler K, Morgenstern B, Zubieta J, Hagrman PJ, Lima N, Sessoli R, Totti F (2004) Angew Chem Int Ed 43:3436–3439
100. Rajaraman G, Murugesu M, Sanudo EC, Soler M, Wernsdorfer W, Helliwell M, Muryn C, Raftery J, Teat SJ, Christou G et al (2004) J Am Chem Soc 126:15445–15457
101. Shoji M, Koizumi K, Kitagawa Y, Kawakami T, Yamanaka S, Okumura M, Yamaguchi K (2006) Chem Phys Lett 432:343–347
102. Bencini A, Totti F (2005) Int J Quant Chem 101:819–825
103. Polo V, Gräfenstein J, Kraka E, Cremer D (2003) Theor Chem Acc 109:22–35
104. Ruiz E, Alvarez S, Cano J, Polo V (2005) J Chem Phys 123:164110
105. Rajaraman G, Totti F, Bencini A, Caneschi A, Sessoli R, Gatteschi D (2009) Dalton Trans 3153–3161
106. Gatteschi D, Sessoli R, Sorace L (2016) Handbook on the physics and chemistry of rare earths, vol 50. Elsevier, pp 91–139
107. Singh SK, Tibrewal NK, Rajaraman G (2011) Dalton Trans 40:10897–10906
108. Efthymiou CG, Stamatatos TC, Papatriantafyllopoulou C, Tasiopoulos AJ, Wernsdorfer W, Perlepes SP, Christou G (2010) Inorg Chem 49:9737–9739
109. Yukawa Y, Aromí G, Igarashi S, Ribas J, Zvyagin S, Krzystek J (2005) Angew Chem Int Ed 44:1997–2001
110. Chibotaru LF (2013) Ab initio methodology for pseudospin Hamiltonians of anisotropic magnetic complexes, chap 6. Wiley, pp 397–519
111. Langley SK, Wielechowski DP, Vieru V, Chilton NF, Moubaraki B, Chibotaru LF, Murray KS (2014) Chem Sci 5:3246–3256
112. Langley SK, Wielechowski DP, Vieru V, Chilton NF, Moubaraki B, Abrahams BF, Chibotaru LF, Murray KS (2013) Angew Chem Int Ed 52:12014–12019
113. Hou X, Nguyen GT, Xu T, Wei H, Herng TS, Huo G, Wang D, Ding J, Wu S, Ungur L, Wu J (2022) Chem Eur J e202200687
114. Miralles J, Daudey J-P, Caballol R (1992) Chem Phys Lett 198:555–562
115. Calzado CJ, Cabrero J, Malrieu JP, Caballol R (2002) J Chem Phys 116:2728–2747
116. Calzado CJ, Cabrero J, Malrieu JP, Caballol R (2002) J Chem Phys 116:3985–4000
117. Castell O, Caballol R (1999) Inorg Chem 38:668–673
118. García V, Castell O, Caballol R, Malrieu J (1995) Chem Phys Lett 238:222–229
119. Calzado CJ, Angeli C, Taratiel D, Caballol R, Malrieu J-P (2009) J Chem Phys 131:044327
120. Singh G, Gamboa S, Orio M, Pantazis DA, Roemelt M (2021) Theor Chem Acc 140:139
121. Aquilante F, Gagliardi L, Pedersen TB, Lindh R (2009) J Chem Phys 130:154107
122. Aquilante F, Pedersen TB, Lindh R (2007) J Chem Phys 126:194106

123. Aquilante F, Boman L, Boström J, Koch H, Lindh R, de Merás AS, Pedersen TB (2011) Cholesky decomposition techniques in electronic structure theory. In: Zalesny R, Papadopoulos MG, Mezey PG, Leszczynski J (eds) Springer Netherlands, Dordrecht, pp 301–343
124. Sierka M, Hogekamp A, Ahlrichs R (2003) J Chem Phys 118:9136–9148
125. Neese F, Wennmohs F, Hansen A, Becker U (2009) Chem Phys 356:98–109
126. Ma D, Manni GL, Gagliardi L (2011) J Chem Phys 135:044128
127. White SR (1992) Phys Rev Lett 69:2863–2866
128. Sharma S, Sivalingam K, Neese F, Chan GK-L (2014) Nat Chem 6:927–933
129. Chan GK-L, Head-Gordon M (2002) J Chem Phys 116:4462–4476
130. Harris TV, Kurashige Y, Yanai T, Morokuma K (2014) J Chem Phys 140:054303
131. Zgid D, Nooijen M (2008) J Chem Phys 128:144116
132. Freitag L, Knecht S, Angeli C, Reiher M (2017) J Chem Theory Comput 13:451–459
133. Phung QM, Muchammad Y, Yanai T, Ghosh A (2021) JACS 1:2303–2314
134. Manni GL, Dobrautz W, Alavi A (2020) J Chem Theory Comput 16:2202–2215
135. Dobrautz W, Weser O, Bogdanov NA, Alavi A, Manni GL (2021) J Chem Theory Comput 17:5684–5703
136. Weser O, Guther K, Ghanem K, Manni GL (2022) J Chem Theory Comput 18:251–272
137. Bogdanov NA, Manni GL, Sharma S, Gunnarsson O, Alavi A (2022) Nat Phys 18:190–195
138. Kahn O, Pei Y, Journaux Y (1989) Mol Cryst Liq Cryst Inc Nonlinear Opt 176:429–441
139. Roos BO, Taylor PR, Sigbahn PE (1980) Chem Phys 48:157–173
140. Andersson K, Malmqvist PA, Roos BO, Sadlej AJ, Wolinski K (1990) J Phys Chem 94:5483–5488
141. Andersson K, Malmqvist P-Å, Roos BO (1992) J Chem Phys 96:1218–1226
142. Schlappa J, Wohlfeld K, Zhou K, Mourigal M, Haverkort M, Strocov V, Hozoi L, Monney C, Nishimoto S, Singh S et al (2012) Nature 485:82–85
143. Walters AC, Perring TG, Caux J-S, Savici AT, Gu GD, Lee C-C, Ku W, Zaliznyak IA (2009) Nat Phys 5:867–872
144. Braicovich L, Ament L, Bisogni V, Forte F, Aruta C, Balestrino G, Brookes N, De Luca G, Medaglia P, Granozio FM et al (2009) Phys Rev Lett 102:167401
145. Coldea R, Hayden S, Aeppli G, Perring T, Frost C, Mason T, Cheong S-W, Fisk Z (2001) Phys Rev Lett 86:5377
146. Booth GH, Thom AJ, Alavi A (2009) J Chem Phys 131:054106
147. Cleland D, Booth GH, Alavi A (2011) J Chem Phys 134:024112
148. Sun Q, Yang J, Chan GK-L (2017) Chem Phys Lett 683:291–299
149. Sharma S, Chan GK-L (2012) J Chem Phys 136:124121
150. Gunnarsson O, Andersen O, Jepsen O, Zaanen J (1989) Phys Rev B 39:1708
151. Gunnarsson O, Jepsen O (1988) Phys Rev B 38:3568
152. Katukuri VM, Bogdanov NA, Weser O, Van den Brink J, Alavi A (2020) Phys Rev B 102:241112
153. Lu H, Rossi M, Nag A, Osada M, Li D, Lee K, Wang B, Garcia-Fernandez M, Agrestini S, Shen Z et al (2021) Science 373:213–216
154. Lin J, Arribi PV, Fabbris G, Botana A, Meyers D, Miao H, Shen Y, Mazzone D, Feng J, Chiuzbăian S et al (2021) Phys Rev Lett 126:087001
155. Lines ME (1971) J Chem Phys 55:2977–2984
156. Ungur L, Chibotaru LF (2006–2022) The computer programs SINGLE_ANISO and POLY_ANISO. University of Leuven
157. Ungur L, Thewissen M, Costes J-P, Wernsdorfer W, Chibotaru LF (2013) Inorg Chem 52:6328–6337
158. Chibotaru LF, Ungur L, Aronica C, Elmoll H, Pilet G, Luneau D (2008) J Am Chem Soc 130:12445–12455
159. Long J, Habib F, Lin P-H, Korobkov I, Enright G, Ungur L, Wernsdorfer W, Chibotaru LF, Murugesu M (2011) J Am Chem Soc 133:5319–5328
160. Vieru V, Ungur L, Cemortan V, Sukhanov A, Baniodeh A, Anson CE, Powell AK, Voronkova V, Chibotaru LF (2018) Chem Eur J 24:16652–16661

161. Chibotaru LF, Girerd J-J, Blondin G, Glaser T, Wieghardt K (2003) J Am Chem Soc 125:12615–12630
162. Prokof'Ev N, Stamp P (1998) Phys Rev Lett 80:5794
163. Leng J-D, Liu J-L, Zheng Y-Z, Ungur L, Chibotaru LF, Guo F-S, Tong M-L (2013) Chem Commun 49:158–160
164. Harriman KL, Le Roy JJ, Ungur L, Holmberg RJ, Korobkov I, Murugesu M (2017) Chem Sci 8:231–240
165. Tian H, Ungur L, Zhao L, Ding S, Tang J, Chibotaru LF (2018) Chemistry (Weinheim an der Bergstrasse, Germany) 24:9928–9939
166. Perfetti M, Gysler M, Rechkemmer-Patalen Y, Zhang P, Taştan H, Fischer F, Netz J, Frey W, Zimmermann LW, Schleid T et al (2019) Chem Sci 10:2101–2110
167. Guo F-S, Liu J-L, Leng J-D, Meng Z-S, Lin Z-J, Tong M-L, Gao S, Ungur L, Chibotaru LF et al (2011) Chem Eur J 17:2458
168. Soncini A, Chibotaru LF (2008) Phys Rev B 77:220406
169. Visinescu D, Madalan AM, Andruh M, Duhayon C, Sutter J-P, Ungur L, Van den Heuvel W, Chibotaru LF (2009) Chem Eur J 15:11808–11814
170. Hewitt IJ, Lan Y, Anson CE, Luzon J, Sessoli R, Powell AK (2009) Chem Commun 6765–6767
171. Lecren L, Wernsdorfer W, Li Y-G, Roubeau O, Miyasaka H, Clérac R (2005) J Am Chem Soc 127:11311–11317
172. Wernsdorfer W, Aliaga-Alcalde N, Hendrickson DN, Christou G (2002) Nature 416:406–409
173. Meng Y-S, Xiong J, Yang M-W, Qiao Y-S, Zhong Z-Q, Sun H-L, Han J-B, Liu T, Wang B-W, Gao S (2020) Angew Chem 132:13137–13143
174. He M, Guo F-S, Tang J, Mansikkamäki A, Layfield RA (2021) Chem Commun 57:6396–6399
175. Wu H, Li M, Xia Z, Montigaud V, Cador O, Le Guennic B, Ke H, Wang W, Xie G, Chen S et al (2021) Chem Commun 57:371–374
176. Wang H-S, Zhou P-F, Wang J, Long Q-Q, Hu Z, Chen Y, Li J, Song Y, Zhang Y-Q (2021) Inorg Chem 60:18739–18752
177. Chibotaru LF, Ungur L, Soncini A (2008) Angew Chem 120:4194–4197
178. Baum M, Schmalzl K, Steffens P, Hiess A, Regnault LP, Meven M, Becker P, Bohatý L, Braden M (2013) Phys Rev B 88:024414
179. Pavlyukh Y (2020) Phys Rev B 101:144408
180. Plokhov DI, Popov AI, Zvezdin AK (2011) Phys Rev B 84:224436
181. Ungur L, Van den Heuvel W, Chibotaru LF (2009) J Chem 33:1224–1230
182. Lin S-Y, Wernsdorfer W, Ungur L, Powell AK, Guo Y-N, Tang J, Zhao L, Chibotaru LF, Zhang H-J (2012) Angew Chem Int Ed 51:12767–12771
183. Novitchi G, Pilet G, Ungur L, Moshchalkov VV, Wernsdorfer W, Chibotaru LF, Luneau D, Powell AK (2012) Chem Sci 3:1169–1176
184. Guo P-H, Liu J-L, Zhang Z-M, Ungur L, Chibotaru LF, Leng J-D, Guo F-S, Tong M-L (2012) Inorg Chem 51:1233–1235
185. Gysler M, El Hallak F, Ungur L, Marx R, Hakl M, Neugebauer P, Rechkemmer Y, Lan Y, Sheikin I, Orlita M et al (2016) Chem Sci 7:4347–4354
186. Rinck J, Novitchi G, Van den Heuvel W, Ungur L, Lan Y, Wernsdorfer W, Anson CE, Chibotaru LF, Powell AK (2010) Angew Chem Int Ed 49:7583–7587
187. Borta A, Jeanneau E, Chumakov Y, Luneau D, Ungur L, Chibotaru LF, Wernsdorfer W (2011) New J Chem 35:1270–1279
188. Bhunia A, Gamer MT, Ungur L, Chibotaru LF, Powell AK, Lan Y, Roesky PW, Menges F, Riehn C, Niedner-Schatteburg G (2012) Inorg Chem 51:9589–9597
189. Langley SK, Chilton NF, Ungur L, Moubaraki B, Chibotaru LF, Murray KS (2012) Inorg Chem 51:11873–11881
190. Feltham HL, Clerac R, Ungur L, Vieru V, Chibotaru LF, Powell AK, Brooker S (2012) Inorg Chem 51:10603–10612
191. Feltham HL, Clerac R, Ungur L, Chibotaru LF, Powell AK, Brooker S (2013) Inorg Chem 52:3236–3240

192. Liu J-L, Wu J-Y, Chen Y-C, Mereacre V, Powell AK, Ungur L, Chibotaru LF, Chen X-M, Tong M-L (2014) Angew Chem Int Ed 53:12966–12970
193. Langley SK, Ungur L, Chilton NF, Moubaraki B, Chibotaru LF, Murray KS (2014) Inorg Chem 53:4303–4315
194. Liu J-L, Wu J-Y, Huang G-Z, Chen Y-C, Jia J-H, Ungur L, Chibotaru LF, Chen X-M, Tong M-L (2015) Sci Rep 5:1–9
195. Langley SK, Le C, Ungur L, Moubaraki B, Abrahams BF, Chibotaru LF, Murray KS (2015) Inorg Chem 54:3631–3642
196. Langley SK, Ungur L, Chilton NF, Moubaraki B, Chibotaru LF, Murray KS (2011) Chem Eur J 17:9209
197. Hayton TW (2013) Chem Commun 49:2956–2973
198. Gardner BM, King DM, Tuna F, Wooles AJ, Chilton NF, Liddle ST (2017) Chem Sci 8:6207–6217
199. McAdams SG, Ariciu A-M, Kostopoulos AK, Walsh JP, Tuna F (2017) Coord Chem Rev 346:216–239
200. Autillo M, Guerin L, Bolvin H, Moisy P, Berthon C (2016) Phys Chem Chem Phys 18:6515–6525
201. Gryaznov D, Heifets E, Sedmidubsky D (2010) Phys Chem Chem Phys 12:12273–12278
202. Dey S, Rajaraman G (2019) J Chem Sci 131:1–13
203. Jung J, Atanasov M, Neese F (2017) Inorg Chem 56:8802–8816
204. Martel L, Islam MA, Popa K, Vigier J-F, Colineau E, Bolvin H, Griveau J-C (2021) J Phys Chem C 125:22163–22174
205. Autillo M, Islam MA, Héron J, Guérin L, Acher E, Tamain C, Illy M-C, Moisy P, Colineau E, Griveau J-C et al (2021) Chem Eur J 27:7138–7153
206. Autillo M, Islam MA, Jung J, Pilmé J, Galland N, Guerin L, Moisy P, Berthon C, Tamain C, Bolvin H (2020) Phys Chem Chem Phys 22:14293–14308
207. Rinehart JD, Long JR (2011) Chem Sci 2:2078–2085
208. Rinehart JD, Fang M, Evans WJ, Long JR (2011) Nat Chem 3:538–542
209. Demir S, Gonzalez MI, Darago LE, Evans WJ, Long JR (2017) Nat Commun 8:1–9
210. Liu F, Krylov DS, Spree L, Avdoshenko SM, Samoylova NA, Rosenkranz M, Kostanyan A, Greber T, Wolter AU, Büchner B et al (2017) Nat Commun 8:1–9
211. Velkos G, Krylov D, Kirkpatrick K, Liu X, Spree L, Wolter A, Büchner B, Dorn H, Popov A (2018) Chem Commun 54:2902–2905
212. Iwahara N, Huang Z, Neefjes I, Chibotaru LF (2022) Phys Rev B 105:144401
213. Gould CA, McClain KR, Reta D, Kragskow JG, Marchiori DA, Lachman E, Choi E-S, Analytis JG, Britt RD, Chilton NF et al (2022) Science 375:198–202
214. Mavragani N, Errulat D, Gálico DA, Kitos AA, Mansikkamäki A, Murugesu M (2021) Angew Chem Int Ed 60:24206–24213